

Copyright Undertaking

This thesis is protected by copyright, with all rights reserved.

By reading and using the thesis, the reader understands and agrees to the following terms:

1. The reader will abide by the rules and legal ordinances governing copyright regarding the use of the thesis.
2. The reader will use the thesis for the purpose of research or private study only and not for distribution or further reproduction or any other purpose.
3. The reader agrees to indemnify and hold the University harmless from and against any loss, damage, cost, liability or expenses arising from copyright infringement or unauthorized usage.

If you have reasons to believe that any materials in this thesis are deemed not suitable to be distributed in this form, or a copyright owner having difficulty with the material being included in our database, please contact lbsys@polyu.edu.hk providing details. The Library will look into your claim and consider taking remedial action upon receipt of the written requests.

The Hong Kong Polytechnic University

Department of Applied Physics

Thickness effects in ferroelectric thin films

Li Kwok Tung

A thesis submitted in partial fulfillment of
the requirements for the Degree of
Master of Philosophy

September, 2004



Pao Yue-kong Library
PolyU · Hong Kong

CERTIFICATE OF ORIGINALITY

I hereby declare that this thesis is my own work and that, to the best of my knowledge and belief, it reproduces no material previously published or written nor material which has been accepted for the award of any other degree or diploma, except where due acknowledgement has been made in the text.

_____ (Signed)

LI Kwok Tung (Name of student)



ABSTRACT

Due to the recent progress of thin film formation techniques, thin film ferroelectric devices are now available. The film thickness is an important parameter for these devices, because it strongly influences the ferroelectric properties and hence the performance of these devices when the film thickness is small.

The aim of this project is to find out the primary cause responsible for various thickness effects observed from experiments. It has been suggested that the presence of surface layers at the electrode/film interface induces these thickness dependence. Unlike previous works assuming these layers to be dielectric (or non-ferroelectric), we proposed that they are ferroelectric with parameters different from those of the interior region of the film.

Our simulation work starts from the four-state Potts model for a two-dimensional array of dipoles, because of the dominance of 90° domains found in many ferroelectric thin films. It implies that the dipole of each cell is restricted only to one of the four states. The coupling coefficient and magnitude of the dipoles at the surface layer are different from those in the interior.

The presence of oxygen vacancies has also been considered to be one of the causes for the thickness dependence. The difference in coupling coefficients at the surface layer can be related to the presence of oxygen vacancies. The different magnitude of dipole moment is caused by the vacancy-induced space charge. An additional energy is



required to rotate a dipole in the presence of an oxygen vacancy in the same cell. Consequently, the coupling coefficient is enhanced.

Hysteresis loops for different thickness have been simulated. The corresponding coercive field and the remanent polarization were obtained. The theoretical results have been compared with experiment (H. Fujisawa, S. Nakashima, K. Kaibara, M. Shimizu, and H. Niu, *Jpn. J. Appl. Phys.*, **38**, 5392 (1999)). Moreover, polarization fatigue has also been simulated. This phenomenon is related to the migration of oxygen vacancies from both electrodes after a number of switching cycles. The reduction of remanent polarization and enhancement of coercive field after many switching cycles, as observed from experiments, have been reproduced.



PUBLICATIONS

1. Kwok Tung Li and Veng Cheong Lo, 'Thickness dependence on the coercive field in ferroelectric thin films', *Journal of the Ceramic Society of Japan (Supplement)*, **112**, S1 (2004).
2. Kwok Tung Li and Veng Cheong Lo, 'Simulation of thickness dependence in ferroelectric thin films', *Solid State Communications*, **132**, 49 (2004).
3. Kwok Tung Li and Veng Cheong Lo, 'Simulation of oxygen vacancy induced phenomena in ferroelectric thin films', *J. Appl. Phys.*, (accepted for publication on November 2004).
4. Kwok Tung Li and Veng Cheong Lo, 'Thickness effects in ferroelectric thin film', (submitted to *Integrated Ferroelectrics*).



ACKNOWLEDGMENTS

I would like to express my sincere gratitude to my supervisor Dr. V. C. Lo, for his illuminating guidance, patient supervision and encouragement throughout my study. I would also like to express my gratitude to Mr. M. T. Lung for his help with my computer simulation. The work described in this thesis is fully supported by the Research Grant Council of the Hong Kong Special Administration Region, China (Project No: G-9051).



TABLES OF CONTENTS

	PAGE
ABSTRACT.....	i
PUBLICATIONS.....	iii
ACKNOWLEDGEMENTS.....	iv
TABLE OF CONTENTS.....	v
LIST OF FIGURES.....	viii
LIST OF SYMBOLS.....	xiii

CHAPTERS

I.	INTRODUCTION.....	1
II.	REVIEWS	
2.1	Studies on Thickness Dependence.....	3
2.2	Studies on Polarization Fatigue.....	6



2.3	Roles of Oxygen Vacancies.....	8
III. THEORETICAL MODEL		
3.1	Formulation of Two Dimensional Potts Model.....	11
3.2	Initialization of Domains.....	16
3.3	Constraint on Polarization Switching.....	21
3.4	Expected Simulation Results.....	27
IV. SIMULATION OF THICKNESS DEPENDENCE IN THE PRESENCE OF SURFACE LAYERS		
4.1	Basic Assumptions.....	31
4.2	Simulation Results and Discussion.....	32
V. PHENOMENA IN FERROELECTRIC THIN FILMS IN THE PRESENCE OF OXYGEN VACANCIES		
5.1	The Role of the Oxygen Vacancy on the Switching of Dipole.....	46
5.2	Mathematical Representation of an Oxygen Vacancy in a Cell.....	49
5.3	Space Charge Induced by Oxygen Vacancy.....	50
5.4	System Hamiltonian in the Presence of Oxygen Vacancies.....	51
5.5	Simulation Results on the Thickness Dependence.....	52
5.6	Simulation Results on Polarization Fatigue and Coercive Field Enhancement.....	60



VI.	CONCLUSION.....	73
	REFERENCES.....	75



LIST OF FIGURES

	PAGE
Fig. 3.1	(a) Initially, there is no dipole inside the film. (b) A prescribed number of seed dipoles are randomly assigned in the film. The state of each seed dipole is also randomly assigned to one of the four states. (c) After the initialization of seed dipoles, the domains are form by capturing the unassigned cells neighbouring to the assigned cells, so that the former have the same state as the latter. (d) Domain “growth” proceeds until all cells have been assigned.....18
Fig. 3.2	In the presence of an assigned cell neighboring to an unassigned cell as shown in (a), the latter cell will be captured and assigned with the same state as the former one. However, for the unassigned cell at the boundary of two different domains (b), there are two assigned cells neighboring to the unassigned cell. In this case, the unassigned cell will be captured by one of them with equal probability. Similarly, in (c) and (d), the unassigned cell will be assigned to one of these domains with equal probability.....19
Fig. 3.3	(a) Plots of polarization against number of MCS for different thicknesses. The numbers of MCS to achieve 99% steady state value for different thicknesses are also shown. (b) Plots of the



	number of MCS to achieve 99% of the steady state polarization against thickness N_z . The number of MCS increases with thickness.....	25
Fig. 3.4	Thickness dependence on coercive field evaluated from (i) Landau-Khalatnikov theory (solid line), (ii) Potts model with period scaled with thickness (dashed line), and (iii) Potts model with unscaled period (dotted line).....	26
Fig. 3.5	Hysteresis loops for different values of periods: (i) $\Gamma = 200$ (solid line), (ii) $\Gamma = 400$ (dashed line), (iii) $\Gamma = 600$ (dotted line), and (iv) $\Gamma = 800$ (dash-dotted line).....	28
Fig. 3.6	Hysteresis loops for different amplitudes of driving electric field e_m : (i) $e_m = 1.0$ (solid line), (ii) $e_m = 1.5$ (dashed line), (iii) $e_m = 2.0$ (dotted line), and (iv) $e_m = 2.5$ (dash-dotted line).....	29
Fig. 3.7	Hysteresis loops at different temperatures (i) $t_n = 0.5$ (solid line), (ii) $t_n = 0.8$ (dashed line), (iii) $t_n = 1.0$ (dotted line), and (iv) $t_n = 1.2$ (dash-dotted line).....	30
Fig. 4.1	Hysteresis loops for difference thicknesses: $N_z = 65$ (solid line), $N_z = 180$ (dashed line), $N_z = 720$ (dotted line), The parameters are: $j_n^S = 1.2$, $p_{on}^S = 0.7$, $j_n^B = 1.0$, $p_{on}^B = 1.0$, $e_m = 0.5$, $t_n = 0.8$, $N_s = 30$	33
Fig. 4.2	Thickness dependence of coercive field for different surface	



	coupling coefficients. The surface dipole moment is set equal to the bulk dipole moment ($p_o^B = 1.0$). Other parameters are the same as in Fig. 4.1.....	35
Fig. 4.3	Thickness dependence of remanent polarization for different surface dipole moments. The surface coupling coefficient is set equal to the bulk coupling coefficient ($j_n^B = 1.0$). Other parameters are the same as in Fig. 4.1.....	36
Fig. 4.4	Polarization profiles across the film of thickness $N_z = 180$ at different times: one-quarter (solid line) and three-quarter (dashed line). The parameters are the same as in Fig. 4.1.....	37
Fig. 4.5	P-E loops at the (a) top interfacial layers, (b) middle layer, (c) bottom interfacial layer. Overall P-E loop for the whole film is shown in (d).....	38
Fig. 4.6	Effect of space charge on the thickness dependence of coercive field (a) $j_n^S = 1.0$ and (b) $j_n^B = 1.2$ with different ρ_{on} values, all other parameters except j_n^S are the same as in Fig. 4.1.....	41
Fig. 4.7	Effect of depolarization on the thickness dependence of coercive field (a) $j_n^S = 1.0$ and (b) $j_n^B = 1.2$ with different γ_n values, all other parameters except j_n^S are the same as in Fig. 4.1.....	43
Fig. 5.1	In the presence of the oxygen vacancy at the top plane, an additional energy H_{p1} is required to displace Ti^{4+} ion from and	



	to the following equilibrium positions: (a) from the bottom to left, (b) bottom to right, (c) left to top, and (d) right to top.....	48
Fig. 5.2	Hysteresis loops for difference thicknesses: $N_z = 100$ (solid line), $N_z = 150$ (dashed line), $N_z = 300$ (dotted line). Other parameters are listed in the text.....	53
Fig. 5.3	Thickness dependence of coercive field e_c for different number of oxygen vacancies N_v	54
Fig. 5.4	Thickness dependence of remanent polarization p_r for different number of oxygen vacancies N_v	55
Fig. 5.5	Thickness dependence of coercive field E_c from (i) experimental result of Fujisawa <i>et al.</i> [9] (solid squares), (ii) simulation result in the presence of oxygen vacancies (dashed line), and (iii) simulation result in the presence of surface layer (dotted line).....	56
Fig. 5.6	Thickness dependence of remanent polarization P_r from (i) experimental result from Fujisawa <i>et al.</i> [9] (solid squares), (ii) simulation result in the presence of oxygen vacancies (dashed line), and (iii) simulation result in the presence of surface layer (dotted line).....	57
Fig. 5.7	Relation between the total number of oxygen vacancies N_v and the surface coupling coefficient j_n^s	59
Fig. 5.8	Plot of coercive field e_c and remanent polarization p_r against	



	the total number of oxygen vacancies N_v	62
Fig. 5.9	A trapping level is induced by an oxygen vacancy. (a) It traps a hole when the position of Fermi level is below and (b) releases a hole when the Fermi level is above the trapping level.....	63
Fig. 5.10	The plot of accumulated charge $\Delta Q/qN_v$ against number of switching cycles N . ($\Gamma = 300\text{MCS}$, $\sigma_t = 0.01\text{MCS}^{-1}$, $e_t = 0.002\text{MCS}^{-1}$)	66
Fig. 5.11	Effect of temperature on polarization fatigue: our simulated results are plotted as curves; experimental results from Panton <i>et al</i> [61] are shown as symbols.....	68
Fig. 5.12	Effect of amplitude of driving voltage on polarization fatigue: our simulated results are plotted as curves; experimental results from Mihara <i>et al.</i> [52] are shown as symbols.....	69
Fig. 5.13	Effect of frequency on polarization fatigue curves: simulated result; symbols: experimental result from Majumder <i>et al.</i> [29].....	70



LIST OF SYMBOLS

c_1	Fitting constant.
c_2	Fitting constant.
c_3	Fitting constant.
c_4	Fitting constant.
c_5	Fitting constant.
D	Average domain size.
d	Thickness of the film.
d_{dep}	Thickness of the depolarization field layer.
d_{SC}	Thickness of the uniform space charge layer.
E_C	Coercive field.
E_{dep}	Depolarization field.
E_F	Fermi energy.
E_m	Applied electric field.
E_{SC}	Charge-induced local electric field.
E_T	Energy of trapping level above the valence band.
E_z	Component of electric field along the z – (thickness) direction.
\hat{E}	Electric field in matrix form.
\hat{E}^T	Transpose of matrix \hat{E} .



e	Normalized electric field.
e_c	Normalized coercive field.
e_{ext}	Normalized external driving electric field.
e_{sc}	Normalized charge-induced local electric field.
e_i	Emission rate of holes by oxygen vacancy.
e_z	Normalized component of electric field along the z – (thickness) direction.
\hat{e}	Normalized electric field in matrix form.
\hat{e}^T	Transpose of matrix \hat{e} .
f	Frequency.
$f(z)$	Distribution function describing the quantity of oxygen vacancies across the thickness of the film.
$f_n(j)$	Normalized distribution function describing the quantity of oxygen vacancies across the thickness of the film.
g_A	Degeneracy factor.
H	Total Hamiltonian energy.
H_o	Coupling energy of oxygen vacancies with the pseudo-spins.
H_b	Coupling energy of oxygen vacancies with the neighboring dipoles.
H_o	Hamiltonian energy in the absence of oxygen vacancies.
H_{P1}	Extra energy for the displacement of Ti^{4+} ion with the presence of an oxygen vacancy in the same cell.



H_{p2}	Extra energy induced from the coupling of the distorted cell with the neighboring dipoles.
h	Normalized total Hamiltonian energy.
h_{p1}	Normalized extra energy for the displacement of Ti^{4+} ion with the presence of an oxygen vacancy in the same cell.
h_{p2}	Normalized extra energy induced from the coupling of the distorted cell with the neighboring dipoles.
i	Index describing the location of a cell in the film along the x – (transverse) direction.
J	Coupling coefficient.
J^B	Bulk coupling coefficient.
J^S	Surface coupling coefficient.
j	Index describing the location of a cell in the film along the z – (thickness) direction.
j_n	Normalized coupling coefficient.
j_n^B	Normalized bulk coupling coefficient.
j_n^S	Normalized surface coupling coefficient.
L_{z1}	Characteristic diffusion length at the top electrode.
L_{z2}	Characteristic diffusion length at the bottom electrode.
N	Number of switching cycles.
N_D	Number of seed dipoles.



N_{dep}	Thickness of the depolarization field layer in terms of number of cells.
N_s	Thickness of the surface layer in terms of number of cells.
N_{sc}	Thickness of the uniform space charge layer in terms of number of cells.
N_v	Total number of oxygen vacancies in the film.
N_v^x	Portion of vacancies without trapping holes.
N_v^+	Portion of charged vacancies.
N_x	Number of dipoles along the x – (transverse) direction.
N_y	Number of dipoles along the y – direction.
N_z	Number of dipoles along the z – (thickness) direction.
N_{z1}	Normalized characteristic diffusion length at the top electrode.
N_{z2}	Normalized characteristic diffusion length at the bottom electrode.
$n(z)$	Number of oxygen vacancies along a transverse monolayer at a distance z from the top surface.
\hat{n}	Normal vector along the electric field direction.
P_o	Magnitude of dipole moment.
P_o^B	Bulk dipole moment.
P_o^S	Surface dipole moment.
P_r	Remanent polarization.
p_o	Normalized dipole moment.



p_o^B	Normalized bulk dipole moment.
p_o^S	Normalized surface dipole moment.
p_r	Normalized remanent polarization.
p_z	Component of normalized polarization along z – direction.
q	Charge.
q_r	Relative charge.
q_{rn}	Normalized relative charge.
r	Random number in the interval (0, 1).
$r(x, z)$	Probability of a vacancy existing in a cell.
\hat{S}	Pseudo-spin matrix represents the orientation of the dipole of a cell.
\hat{S}^T	Transpose matrix of \hat{S} .
T	Temperature.
t	Physical time.
t_{MCS}	Time in Monte Carlo Steps.
t_n	Normalized temperature.
V^X	Neutral oxygen vacancy.
V^+	Charged oxygen vacancy.
\hat{V}	Pseudo-spin matrix representing the location of an oxygen vacancy in a cell.
$x -$	Transverse direction.
$y -$	Longitudinal direction.



z	Thickness direction.
z_n	Normalized depth of thickness.
α	Integrating constant.
Δh	Change in Hamiltonian energy.
ΔQ	Accumulated space charge.
Δz	Thickness of each layer.
ε_o	Dielectric permittivity of vacuum.
ε_r	Relative dielectric permittivity.
Γ	Physcial period.
Γ_{MCS}	Normalized period.
γ	Depolarizing factor.
γ_n	Normalized depolarizing factor.
ρ_o	Uniform charge density.
ρ_{on}	Normalized uniform charge density.
ρ_{sc}	Local charge density.
σ_i	Capture rate of holes by oxygen vacancy.
τ	Switching time (the time required to achieve 99% of the steady state value).
τ_{MCS}	Switching time in Monte Carlo Steps.



CHAPTER I

INTRODUCTION

Due to the recent progress in the techniques of the fabrication of thin film, the formation of quality ferroelectric thin films in nanometer scale is possible. These films are now widely used in microelectronic devices such as non-volatile memory, volatile memory, and electromechanical devices. The major advantages of using ferroelectric thin films include the high switching speed, high density and long endurance [1]. On the other hand, the physical properties of thin films are completely distinct from their bulk counterpart. In particular, the dielectric permittivity, remanent polarization, and coercive field vary with film thickness [2, 3]. From the scientific point of view, it is interesting to pursue the dominant mechanisms that influence the ferroelectricity when the film thickness is small.

The issue of thickness dependence in ferroelectric films has been studied extensively by both experimental investigations and theoretical modelings. In particular, the existence of a surface layer near the electrode/film interface has been suggested. As the film thickness decreases, the role of the electrode/film interface becomes more important. It is natural for many authors to consider the electrode/film interface as the major cause for the thickness effect. The problems are: what is the nature of this surface layer and how it influences the ferroelectric properties.

Because of the distinctive nature of the surface layer, we suggest a different set of coupling coefficient and magnitude of dipole moment for the dipoles inside the surface



layer. The coupling coefficient at the surface layer is larger than that in the bulk while the magnitude of the dipole moment is smaller. Detailed justification of this model and the simulation results will be presented in chapter IV.

Looking into more details about the surface layer, experiments concluded the accumulation of oxygen vacancies in this layer. The presence of oxygen vacancies is one of the reasons for the differences in coupling coefficient and dipole moment in the surface layer. The difference in tetragonalities and the presence of strain are other reasons. The role of oxygen vacancies is: (i) to modify the switching behavior of a dipole in a cell and (ii) to screen the external electric field. Detailed description will be presented in chapter V.

Polarization fatigue is one of the degradation problems where the switchable polarization is reduced after a number of switching cycles [4-7]. It has been generally accepted that polarization fatigue is closely related with the presence of oxygen vacancies. In some experiments, the enhancement of coercive field was also observed in fatigued samples [4]. The presence of space charge has been considered to be the cause of polarization fatigue [8], but its presence alone is not enough to explain the enhancement of coercive field. In this work, we propose that the increase in oxygen vacancies leads to both reduction in remanent polarization and enhancement of coercive field. This increase is a consequence of diffusion of oxygen vacancies from electrodes. Furthermore, the trapping and detrapping of charge carriers by vacancies govern the temporal evolution of space charge, leading to the switching cycle-dependent space charge distribution. The detailed charge trapping mechanism, together with the temperature, frequency, and driving voltage dependent fatigue behaviors will also be discussed in chapter V.



CHAPTER II

REVIEWS

2.1 Studies on Thickness Dependence

Thickness dependence of ferroelectric properties has been extensively studied. There are quite a number of experiments reporting that coercive field increases on decreasing the film thickness. On the other hand, remanent polarization has a monotonic increasing trend with thickness. The works of Fujisawa *et al.* [9], Lin *et al.* [10] and Kundu *et al.* [11] on $\text{Pb}(\text{Zr},\text{Ti})\text{O}_3$ (PZT) thin films grown on different electrodes have confirmed the decreasing trend of coercive field with thickness. Huang *et al.* [12] have obtained a similar trend in BaTiO_3 (BTO) films.

Unlike the results observed in PZT or BTO films, the thickness dependence of coercive field in $0.8\text{SrBi}_2\text{Ta}_2\text{O}_9 - 0.2\text{Bi}_3\text{TiNbO}_9$ (SBT - BTN) films exhibits a different trend [13]. Ducharme *et al.* [14] have studied the ferroelectric properties in PVDF films and discovered that the coercive field stops increasing after the thickness is smaller than a critical value. Moreover, from some experiments in ferromagnetic systems [15, 16], there are two different trends on the size effects of coercive field separated by a critical size. When the size is smaller than the critical value, the coercive field (or switching field) increases monotonically with size. For a size larger than the critical value, decreasing trend takes over. Wei and Choi [16] suggested that the magnetic bar of width smaller than the critical value is essentially in single-domained configuration. For a width larger than the critical value, it becomes multi-domained. The different switching mechanisms for



these two regions lead to different trends of size effects. Because of the similarity between ferroelectricity and ferromagnetism, it is worthwhile to compare the thickness dependence of coercive field from these two systems.

There are two major sources contributing to the thickness effects: intrinsic and extrinsic. Ferroelectricity is a result of collaborative effect contributed by a number of dipoles. This number must be large enough in order to withstand against the depolarizing effects. One example for this depolarizing effect is thermal agitation. This dictates the size-dependent critical temperature for the onset of ferroelectricity. There are also a number of papers in literature discussing the existence of a critical size, below which ferroelectricity disappears [17-19]. The collaborative effect of dipoles comprises the intrinsic cause of thickness dependence. Moreover, a surface layer near the electrode/film interface exists. Under the influence of the interface, the surface layer exhibits physical properties different from those in the bulk. This is the extrinsic cause as this influence can be modified by the selection of electrode materials and by the fabrication process. Tagenstev *et al.* [20] suggested that the surface layer is dielectric in which the spontaneous polarization vanishes. It screens the external electric field by the injected charge. They have also derived the coercive field in the ferroelectric medium:

$$E_C = E_{Co} + \frac{d}{L} E_{th} \quad (2.1)$$

where d is the thickness of the dielectric layer, L the film thickness and E_{th} the threshold field defined in their article. Larsen *et al.* [21] proposed the formation of “blocking layer” by the accumulation of oxygen vacancies after the electrode deposition.



Again, this “blocking layer” was considered to be non-ferroelectric. Baudry *et al.* [22] suggested the presence of a depolarization effect in ferroelectric film. This depolarization was induced by the surface bound charge. They have derived the thickness dependence of coercive field by the two dimensional lattice model based on Landau-Devonshire theory.

In addition to the explanation by the presence of a surface layer, numerous experiments have attributed the thickness dependence of coercive field to the presence of oxygen vacancies. For example, Ma *et al.* [23] have observed the accumulation of oxygen vacancies in the lead-rich surface layers of PbTiO_3 thin film grown on SrTiO_3 substrates. Moreover, the coercive field of PbTiO_3 thin film is larger than the value in bulk PbTiO_3 sample. Tagantsev *et al.* [24] have investigated the thickness dependence of coercive field for both Pt/PZT/Pt and $\text{RuO}_2/\text{PZT}/\text{RuO}_2$ systems. They could observe the expected thickness dependence in Pt/PZT/Pt capacitor, but similar trend disappeared in $\text{RuO}_2/\text{PZT}/\text{RuO}_2$ system. It is suggested the formation of metallic electrodes leads to the accumulation of oxygen vacancies near the electrode/film interface. We will elaborate the role of oxygen vacancy in section 2.3.

For the theoretical explanation on the increasing trend of coercive field with thickness at small thickness, the presence of depolarization field at the electrode/film interface has been attributed as one of the causes. It is expected that the influence of this depolarization field becomes important as the film thickness is very small. In a previous work [25], the coercive field is reduced by the depolarization field. This argument implies the existence of the increasing trend for very small thickness. Richards *et al.* [26] have studied the size effect on nanoscale ferromagnets using Kinetic Ising model. Similar to



the experimental observation mentioned before, they obtained two different regimes of size effect. For small size, the switching field increases with size, but for large size, decreasing trend takes over. Unlike ferromagnetism, the corresponding experimental observation and theoretical modeling on the thickness dependence of coercive field in very thin ferroelectric films are still rare. Mitoseriu *et al.* [27] have studied the grain-size effects of barium titanate using Landau Ginzburg free energy approach. With the additional term to control the size effect, they also obtained the increasing trend of the coercive field with grain size. Bune *et al.* [28] have investigated the ferroelectric properties of crystalline Langmuir-Blodgett-deposited P(VDF - TrFE 70 : 30) polymeric films. The coercive field decreases when the number of monolayers is reduced. To observe similar effect in perovskite films, it is necessary to improve thin film deposition techniques to obtain quality films with such a small thickness.

2.2 Studies on Polarization Fatigue

In polarization fatigue, the switchable polarization is reduced after repeated application of the driving field. Majumder *et al.* [29] suggested that the switchable polarization follows stretched exponential decay with switching cycles. Warren *et al.* [4] have observed the reduction in the remanent polarization in electrically, optically and thermally fatigued film.

Numerous reports have suggested that oxygen vacancy plays an important role on polarization fatigue. In particular, Law *et al.* [30] have observed the increase in fatigue free cycles with increasing oxygen partial pressure during the formation of the RuO_x



electrodes. Obviously, increasing the oxygen composition in the electrode leads to the reduction of oxygen vacancies which ultimately enhances the fatigue resistance. Scott *et al.* [31] have observed the reduction of the oxygen composition near the electrodes after fatigue, reflecting an increase in oxygen vacancy concentration there. For the detailed mechanism imposed by oxygen vacancies on the polarization fatigue, many authors have suggested the pinning of domain walls. The movement of domain walls is believed to be the dominant switching mechanism in a poly-domained sample. For example, Park *et al.* [7] have simulated the pinning effect of oxygen vacancy from a first-principles calculation. He *et al.* [32] concluded that domain-wall pinning is not possible when the vacancy concentration is low. When the concentration becomes large, domain-wall pinning is the dominant mechanism for the reduction of switchable polarization.

The trapping of charge carriers by oxygen vacancies can also induce polarization fatigue. Dimos *et al.* [33] suggested that polarization fatigue is a result of the imbalance between the charge trapping and detrapping rate: an increase of charged vacancies takes place after repeated switching cycles if the first rate is larger than the second one. Similar relation can be found from the work of Dawber *et al.* [34]. They have derived the decrease in switched charge per unit area $P(N)$ due to electromigration of oxygen vacancies from the electrode/film interface. Majumder *et al.* [29] have also presented a similar result.

Besides the reduction of remanent polarization, the coercive field also changes with the number of switching cycles simultaneously. However, there is still no unequivocal conclusion on the change of coercive field. In some experiments [4, 35], the



coercive field was found to be increased with switching cycles, for samples with metal electrode. It has also been reported that the coercive field decreases with switching cycles for samples with oxide electrode [36]. Ricinschi *et al.* [37] have observed that the coercive field decreased after 10^7 switching cycles in sol-gel derived PZT thin film, but increased in the sputtered PZT thin film. They suggested that the fatigue mechanism for sol-gel film is mainly caused by space charge accumulation, while the mobile charged defects is the dominant cause in sputtered film. Consequently, the mobility of charged defects plays an important role on enhancement of coercive field. Majumder *et al.*'s work [29] also support the influence of the mobility of defects on the enhancement or reduction of coercive field during polarization fatigue. In their experiment, they observed the coercive field increased in an undoped/ fatigued PZT film but decreased in the cerium-doped film. The size of Ce^{4+} ion is larger than both Ti^{4+} and Zr^{4+} ion. Even though it is an isovalent substitution, when cerium is doped into the film, the empty space within the lattice is reduced. The mobility of oxygen vacancies is then reduced. As a result, oxygen vacancies, the very species responsible for the enhancement of coercive field, cannot reach the interior region of the film. Furthermore, the formation of surface layer during repeated switching has also been attributed to the enhancement of coercive field. This surface layer has been considered as having a lower dielectric constant [4], depleted from charge carrier [38], or filled with microcracks [39].

2.3 Roles of Oxygen Vacancies



Based on the above discussion, both the polarization fatigue and thickness dependence have been attributed to the presence of oxygen vacancies [23-24, 29-31]. Understanding the role of oxygen vacancy on the polarization switching is the key issue to explain the causes of these phenomena. Oxygen vacancy is a point defect that disturbs the continuity of a lattice. Consequently, it acts as an impedance for the domain wall movement. Domain wall pinning [7, 32] by oxygen vacancies thus reduces the switchable polarization. Lo [40] has described the coupling mechanism between oxygen vacancy and the dipole induced by a perovskite cell. The dipole moment of the latter is contributed by the displacement of Ti^{4+} ion away from the centre of symmetry. In the presence of an oxygen vacancy at the edge of the perovskite cell, it demands an additional energy to displace the Ti^{4+} ion from an equilibrium position apart from the oxygen vacancy to the other equilibrium position near the oxygen vacancy. Thus the dipole moment has a preferential direction imposed by the oxygen vacancy and the switching by reversing the dipole orientation is more difficult. On the other hand, oxygen vacancy can also trap or emit charge carrier to become a space charge [33, 35, 40]. This space charge creates a non-uniform electric field distribution over the thickness. In this region deep inside the film, even without the “pinning” effect imposed by oxygen vacancies, dipoles are not able to flip in response to the external driving field because of the screening effect induced by the space charge layer. Moreover, the distribution of oxygen vacancies is inhomogeneous such that they are accumulated at the surface layers beneath the electrode/film interface. The thickness of this surface layer is determined by the quantities of oxygen vacancies and by other inhomogeneities such as strain and



tetragonality [25]. This thickness does not necessarily decrease proportionally with the film thickness. As mentioned before, thickness dependence of coercive field has been attributed to the presence of this surface layer. The smaller the film thickness, the thickness dependence is more pronounced. The nature of this surface layer has been suggested to be dielectric (or paraelectric), where the spontaneous polarization is absent. Larsen *et al.* [21] and Stolichnov *et al.* [41] moved closer to relate the accumulation of oxygen vacancies at the surface layer and the thickness dependence. In this thesis, we will describe the roles of oxygen vacancy on the dipolar switching and on the charge exchange. These two microscopic mechanisms lead to various observable phenomena in ferroelectric thin films, such as thickness effects and polarization fatigue. Jin *et al.* [42] have investigated the fatigue behavior and thickness dependence over a wide range of ferroelectric film/electrode combinations experimentally. They found that both size effect and fatigue behavior occurred simultaneously in PZT, BST, and BT films with metal electrodes but disappeared in these samples with oxide-electrodes. This reflects that both polarization fatigue and thickness dependence may be caused by the same origin. These authors have also suggested that although the dead-layer approach has been traditionally used to account for the size effects, no experimental evidence has so far been found. On the other hand, oxygen vacancy is the dominant defect species in metal-electroded films.



Chapter III

THEORETICAL MODEL

3.1 Formulation of Two Dimensional Potts Model

In this work we have adopted the two-dimensional q -state Potts model with $q = 4$. The q -state Potts model is a generalization of the Ising model, with q metastable states instead of two. Experiments have shown the existence of both 90° and 180° domain walls in perovskite-type thin ferroelectric films [43], even in single crystalline samples. It is reasonable to consider that there are four different dipole orientations, mutually perpendicular to each other. Compared with the Ising model, the four-state Potts model provides a more realistic scenario to simulate the multi-domained ferroelectrics. Moreover, Liu *et al.* [44] have made a comparison between the Ising model and the Potts model. They conclude that the Ising model produces a square hysteresis loop, while the Potts model generates a rhombic hysteresis loop, which is closer to experimental results. In fact, using the two-dimensional four-state Potts model to simulate ferroelectric properties can be found elsewhere in the literature. For example, Qian *et al.* [45] have successfully simulated dielectric breakdown in PMN-PT film using two-dimensional four-state Potts model. Liu *et al.* [46] have studied the frequency dependence of the hysteresis loop area using the two-dimensional Potts model.

As has been mentioned in the last chapter, the presence of oxygen vacancy in a perovskite cell affects the displacement of Ti^{4+} ion, and hence the polarization switching. Lo [8] has simulated the ferroelectric properties using Ising model in the presence of



oxygen vacancies. In his model, he considered only two possible directions for each of the dipoles in the film. Consequently, only the oxygen vacancies located either at the top or at the bottom of the cell affect the switching of the dipole. There are six possible directions for the displacement of a Ti^{4+} ion: two vertical and four transverse, resulting in six possible dipole orientations. For a ferroelectric sample in tetragonal phase, the symmetry property belongs to $4mm$ group. With the elongated edge of the perovskite cell along the vertical (or z -axis) direction, any effect taking place along the front or back (or y -axis) direction is similar to that along the left and right (or x -axis) direction. Thus, keeping only four states in a two-dimensional geometry for the dipole orientations may be adequately enough. Oxygen vacancy can also be located at any one of the six faces of the cell. By the same token, considering only those located at the left, right, top and bottom faces of the cell is enough. The interaction of the dipole with oxygen vacancy located at all of these positions should be taken into account. The coupling can be easily handled by using the four-state Potts model but is more difficult by the Ising model.

In the four-state Potts model, the ferroelectric thin film can be represented by a two-dimensional array of dipoles. The size of the array is $N_x \times N_z$, where N_x and N_z are the numbers of dipoles along the x - (transverse) and z - (thickness) directions, respectively. The displacement of the Ti^{4+} ion in each cell gives a dipole moment. The elongated edge of the cell is along the z -axis. As the electric field is applied along the thickness direction, we assume that the variation in ferroelectric properties vary only along the thickness direction.



A monolayer is a layer with a thickness equal to the elongated edge of a tetragonal perovskite cell, Δz . The thickness of the film is thus $d = N_z \Delta z$.

The location of a cell in the film can be described by a pair of indices (i, j) , where $0 < i \leq N_x$ and $0 < j \leq N_z$. The orientation of the dipole of this cell is denoted by a state variable called the pseudo-spin matrix $\hat{S}_{i,j}$ with the following values:

$$\begin{aligned} \hat{S}_A &= \begin{bmatrix} 1 \\ 0 \end{bmatrix} \text{ (upward),} & \hat{S}_B &= \begin{bmatrix} 0 \\ 1 \end{bmatrix} \text{ (left),} \\ \hat{S}_C &= \begin{bmatrix} -1 \\ 0 \end{bmatrix} \text{ (downward),} & \hat{S}_D &= \begin{bmatrix} 0 \\ -1 \end{bmatrix} \text{ (right), and} \\ \hat{S}_0 &= \begin{bmatrix} 0 \\ 0 \end{bmatrix} \text{ (Dipole is absent)} \end{aligned} \quad (3.1)$$

The last spin state \hat{S}_0 only exists at the top or bottom electrodes.

In our simulation, our aim is to study the thickness dependence of ferroelectric properties. Consequently, we consider films of infinite transverse size and a finite thickness along the z -direction. We adopt periodic boundary condition for the transverse edges, and free boundary condition for the top and bottom electrodes, as follows:

$$\hat{S}_{0,j} = \hat{S}_{N_x,j}, \quad \hat{S}_{N_x+1,j} = \hat{S}_{1,j}, \quad \begin{array}{l} \text{(Periodic boundary condition along} \\ \text{the transverse direction)} \end{array} \quad (3.2)$$

$$\hat{S}_{i,0} = \hat{S}_{i,N_z+1} = \begin{bmatrix} 0 \\ 0 \end{bmatrix}. \quad \begin{array}{l} \text{(Free boundary condition along the top and} \\ \text{bottom electrodes)} \end{array} \quad (3.3)$$



In the q – state Potts model, the Hamiltonian of the interacting spins can be generally expressed as [47]

$$H = -\sum_{i,j} J(\theta_{i,j}), \quad (3.4)$$

where $J(\theta_{i,j})$ is the coupling function, $\theta_{i,j} = \theta_{n_i} - \theta_{n_j}$ the angle between two spin states n_i and n_j , $\theta_n = 2\pi n/q$, and $n < q-1$. Wu [47] discussed two different ways of expressing the coupling coefficient in Potts model: the standard and the planar Potts model. For the former one, the coupling function $J(\theta_{i,j})$ can be written as

$$J(\theta_{i,j}) = \varepsilon_2 \delta_{Kr}(n_i, n_j), \quad (3.5)$$

where

$$\delta_{Kr}(v_1, v_2) = \frac{1}{q} [1 + (q-1)e^{v_1} e^{v_2}], \quad (3.6)$$

$v_1, v_2 = 0, 1, \dots, q-1$, e^{v_1} and e^{v_2} are q unit vectors pointing toward q symmetric directions of a hypertetrahedron, and ε_2 is a constant. For the planar Potts model, the coupling function $J(\theta_{i,j})$ is given by

$$J(\theta_{i,j}) = \varepsilon_1 \cos(\theta_{i,j}), \quad (3.7)$$

where ε_1 is another constant. The second model is not applicable when $q > 4$. However, the standard Potts model can be applied for all q . Moreover, both models are equivalent for $q = 2, 3, 4$.

In our present case with $q = 4$, we have chosen the planar Potts model for simplicity. The possible orientations for each of the spins are: $\theta_n = 0, \pi/2, \pi, 3\pi/4$, for



$n = 0, 1, 2$, and 3 respectively. From Eqn. (3.7), the coupling function $J(\theta_{i,j})$ returns the following values: $J(\theta_{i,j}) = \varepsilon_1 \cos(\theta_{i,j}) = \varepsilon_1$ if the two interacting spins are parallel, $-\varepsilon_1$ anti-parallel, and 0 perpendicular. Moreover, the coupling function also returns zero if one of the interacting spins is at the top or bottom electrodes. We can replace such description by the product of two matrices. If $\hat{S}_{i,j}^T$ represents the transpose matrix of $\hat{S}_{i,j}$, then the coupling function as expressed in Eqn. (3.7) can be replaced by $\{\hat{S}_{i,j}^T \hat{S}_{k,m}\}$. It returns one of the following values for different relative orientation between $\hat{S}_{i,j}$ and $\hat{S}_{k,m}$: $+1$ for parallel, -1 for anti-parallel, and 0 for perpendicular orientation or one of the interacting spins being at the top or bottom electrodes. The Hamiltonian of the system is then given by

$$H_o = - \sum_{i,j,k,m} J \{\hat{S}_{i,j}^T \hat{S}_{k,m}\} - \sum_{i,j} P_o \{\hat{E}_j^T \hat{S}_{i,j}\}, \quad (3.8)$$

where J is the coupling coefficient, P_o the magnitude of the dipole moment, \hat{E}_j is the matrix representation of the electric field, and \hat{E}_j^T is the transpose matrix of \hat{E}_j . In the first term of Eqn. (3.8), only the nearest neighbor interactions are included for simplicity. The second term in Eqn. (3.8) represents the coupling between dipole and the electric field \hat{E}_j . If the external driving field is along z -direction, \hat{E}_j can be explicitly expressed by:

$$\hat{E}_j = \begin{bmatrix} E_z \\ 0 \end{bmatrix}, \quad (3.9)$$



The last term in Eqn. (3.8) returns the value of $+P_o E_z$ when the pseudo-spin is along the $+z$ -direction, $-P_o E_z$ when it is along the $-z$ -direction, and zero otherwise.

The above variables are normalized to dimensionless variables according to the following relations:

$$\begin{aligned} h &= H / J^B, & e_z &= E \times P_o / J^B, & \hat{e} &= \begin{bmatrix} e_z \\ 0 \end{bmatrix}, \\ t_n &= kT / J^B, & j &= z / \Delta z. \end{aligned} \quad (3.10)$$

where J^B is the coupling coefficient in the bulk. After the conversion, the normalized Hamiltonian now becomes

$$h = - \sum_{i,j,k,m} \{ \hat{S}_{i,j}^T \hat{S}_{k,m} \} - \sum_{i,j} \{ \hat{e}_j^T \hat{S}_{i,j} \}. \quad (3.11)$$

3.2 Initialization of Domains

The spin configuration of the film is initialized from an unpoled condition as shown in Fig. 3.1a. The average domain size D , is related to the thickness by:

$$D = c_3 \times \sqrt{N_z}, \quad (3.12)$$

where c_3 is a constant. This relation has been confirmed by experiments [48]. A number of seed dipoles equal to N_D are randomly allocated in the film, where

$$N_D = \frac{N_z}{c_3 \times \sqrt{N_z}} = c_4 \times \sqrt{N_z}. \quad (3.13)$$

The steps of allocating the seed dipoles is shown in Fig. 3.1b. The state of each allocated seed dipole is also randomly assigned to one of the four states. After the assignment of



states for all these seed dipoles, domains are formed by aligning the unassigned cells neighboring to the assigned cells with the same state as shown in Fig. 3.1c. However, for the unassigned cell at the boundary of two different domains as shown Fig. 3.2b, there are two possibilities for the unassigned cell to be aligned with. In this case, the unassigned cell will be aligned to one of these two domains with equal probability. Similar assignment of state for an unassigned cell with neighboring cells of three (Fig. 3.2c) or even four (Fig. 3.2d) different states follows a similar rule. The “growth” proceeds until the states of all the cells have been assigned (Fig. 3.1d).

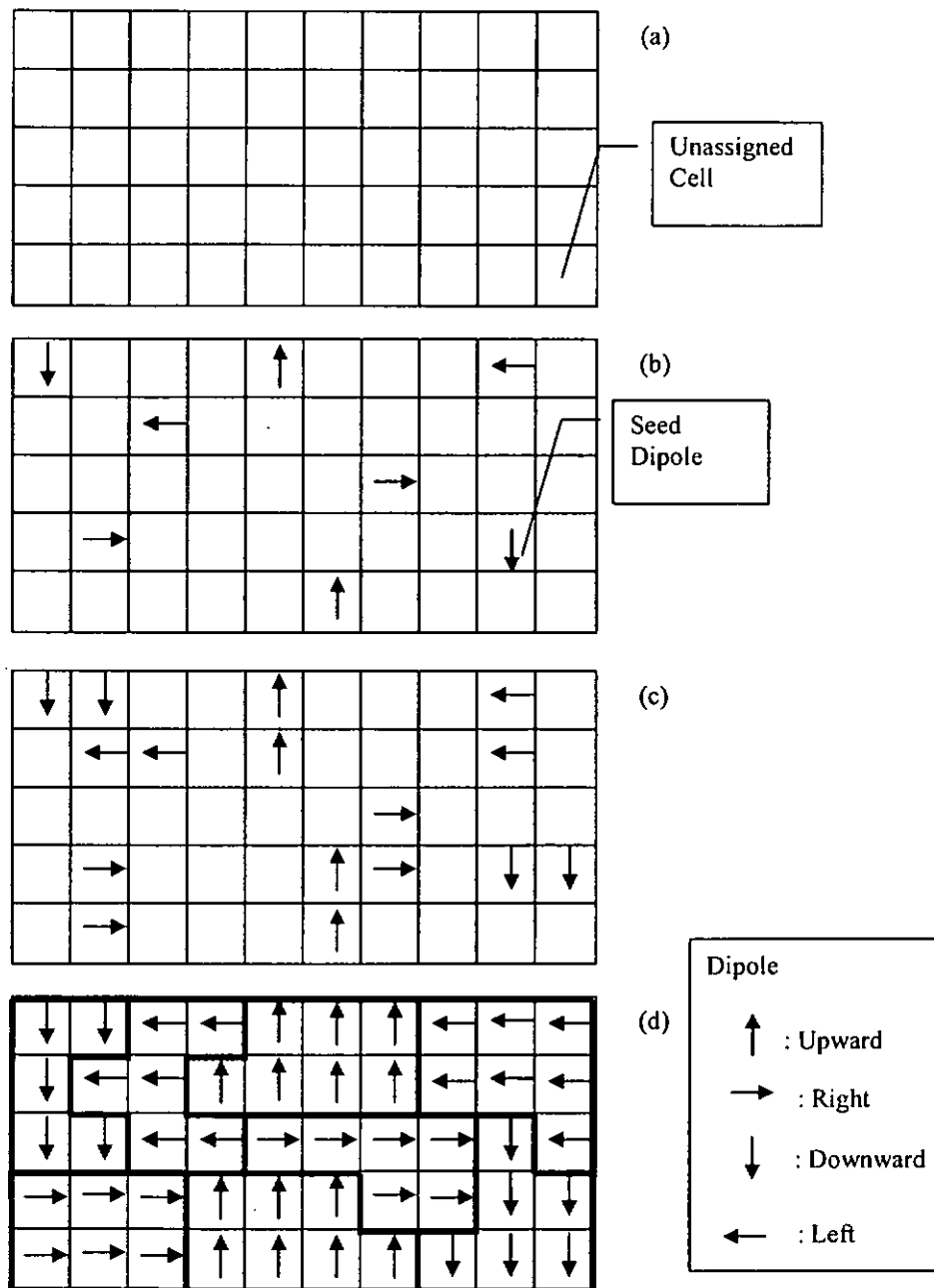
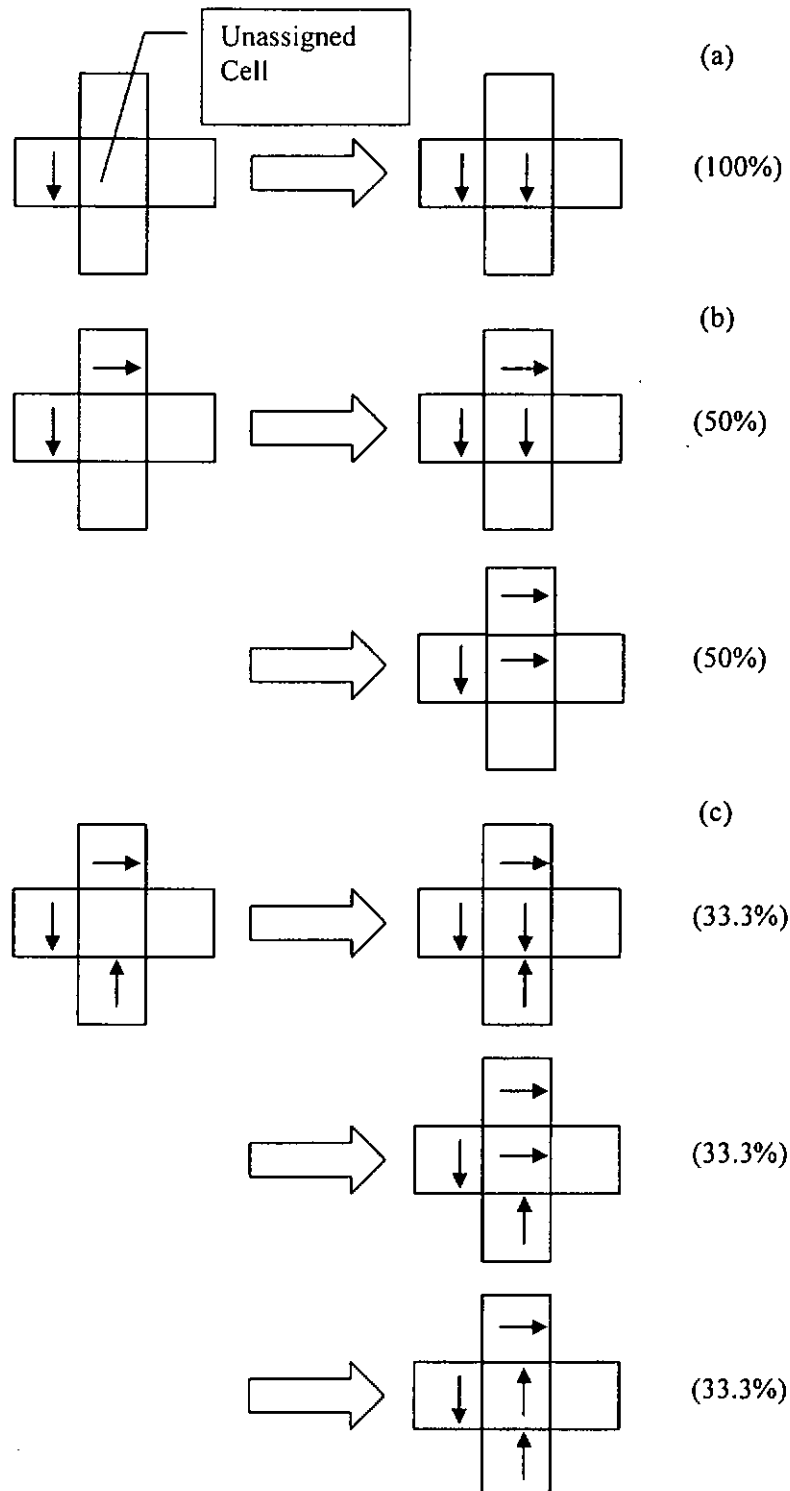


Fig. 3.1 (a) Initially, there is no dipole inside the film. (b) A prescribed number of seed dipoles are randomly assigned in the film. The state of each seed dipole is also randomly assigned to one of the four states. (c) After the initialization of seed dipoles, the domains are formed by capturing the unassigned cells neighbouring to the assigned cells, so that the former have the same state as the latter. (d) Domain "growth" proceeds until all cells have been assigned.



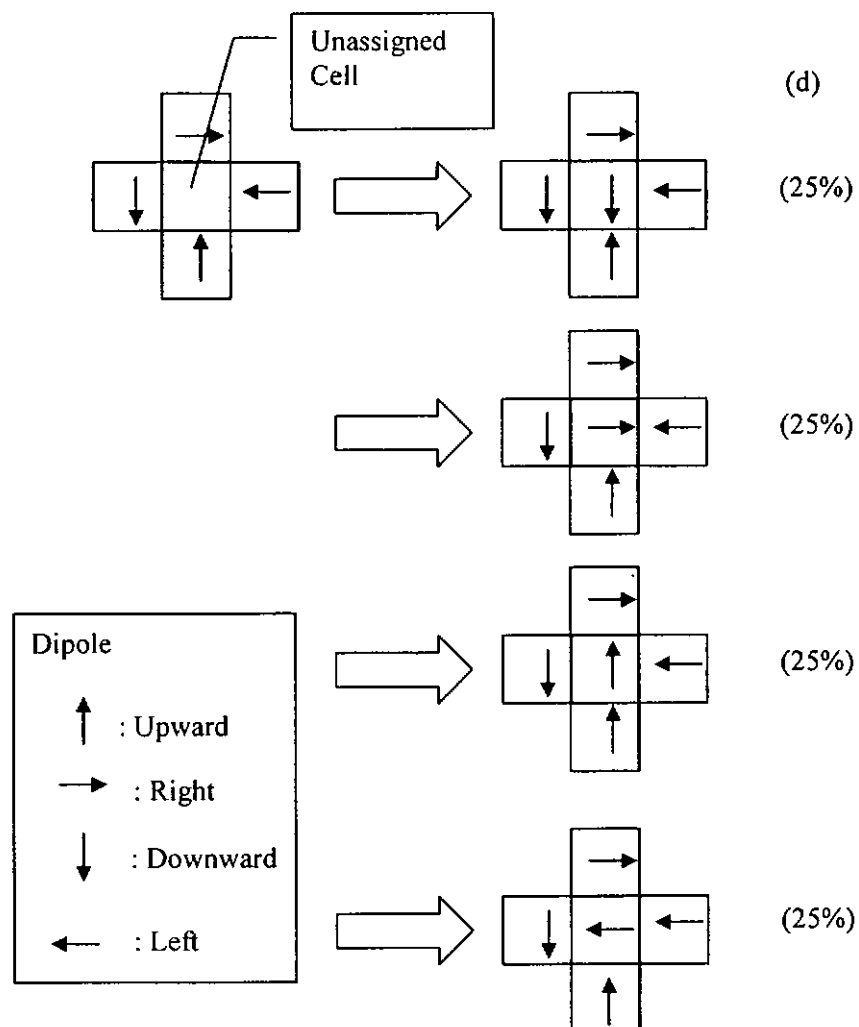


Fig. 3.2 In the presence of an assigned cell neighboring to an unassigned cell as shown in (a), the latter cell will be captured and assigned with the same state as the former one. However, for the unassigned cell at the boundary of two different domains (b), there are two assigned cells neighboring to the unassigned cell. In this case, the unassigned cell will be captured by one of them with equal probability. Similarly, in (c) and (d), the unassigned cell will be assigned to one of these domains with equal probability.



3.3 Constraint on Polarization Switching

In our simulation, we define a Monte Carlo Step (MCS) as the trial of flipping one dipole at a site. We restrict the dipole to undergo a 90° rotation, either clockwise or counter-clockwise, for each trial MCS. For a purely c -domain oriented film, the only possible switching mechanism is by 180° flipping of dipoles. In the co-existence of both a - and c -domains, it is expected that both 90° rotation and 180° flipping occur. The existence of 90° domain walls must be a consequence of 90° rotation of dipoles, even though the external driving field is uniaxial. On the other hand, the presence of 180° domain walls can be caused by either one 180° bipolar flipping or two successive 90° rotations. Nagarajan *et al.* [43] have attributed the enhanced activation field and coercive field of PZT film to the dominance of c -domains under small thickness. Kim *et al.* [49] have also shown that the PZT film with high Ti-content exhibits higher coercive field. This PZT film is in tetragonal phase with (001) orientation. Consequently, the domain switching through 180° flipping of dipoles demands more energy than that by 90° rotation. When both 90° rotation and 180° flipping exist in a film, 90° rotation will then be dominant because it demands less energy, provided that the populations of both 90° and 180° domain walls are comparable. Consequently, in our simulation, we restrict the switching of dipole in each MCS only to 90° rotation.

The polarization switching is implemented by the conventional Metropolis algorithm. At each MCS, a pseudo-spin $\hat{S}_{i,j}$ in the film is randomly chosen. A trial rotation for this spin is tested as follows. The selected pseudo-spin is rotated by 90°



either clockwise or counter-clockwise, with equal probability. The change in Hamiltonian Δh after the rotation is evaluated. The rotation is accepted if $\Delta h < 0$ or $\exp(-\Delta h/t_n)$ where r is a random number in the interval $(0, 1)$, t_n and Δh are the normalized temperature and change in Hamiltonian defined in Eqns. (3.10) and (3.11), respectively. This algorithm ensures that the change in system energy is either minimized or thermally activated under a finite temperature. The spin configuration is then updated. The z – component of the polarization is evaluated as follows:

$$p_z = \frac{\sum_{i,j} \{\hat{S}_{i,j}^z \hat{n}\}}{N_x N_z}, \quad (3.14)$$

where \hat{n} is the unit matrix $\hat{n} = \begin{pmatrix} 1 \\ 0 \end{pmatrix}$.

In order to generate a hysteresis loop, the system is driven by an external alternating field with which the time-dependent polarization is correlated. The number of computational steps must be scaled with some characteristic time of the system. Considering an initially unpoled system subject to a positive DC field, dipoles inside the film rotate sequentially in response to the driving field. The overall polarization gradually increases until it finally attains a steady state value. A switching time τ is then defined as the time required to achieve 99% of the steady state value. It can be found from both experiments and theory that this switching time is independent of the system size [50, 51]. On the other hand, as shown in Fig. 3.3, we can find that the number of MCS to achieve 99% of the steady value increases with increasing thicknesses N_z . Since, the switching time is independent of size, as mentioned before, we must find a relation between the



switching time and the number of MCS to achieve 99% steady value. The time variable is then converted into the number of MCS from this relation in order to perform our simulation. From our simulation, the number of MCS τ_{MCS} to achieve 99% steady value is related to the size by the following relation:

$$\tau_{MCS} = c_1 \times (N_z)^{c_2}, \quad (3.15)$$

where $c_1 = 24,796$ and $c_2 = 0.947$ are fitting constants. The subscript “MCS” denotes the time used in our simulation in terms of number of MCS. All other physical times must be scaled by the factor τ_{MCS} / τ . For example, an alternating external field applied to the system can be converted into

$$E = E_m \sin\left(\frac{2\pi t}{\Gamma}\right) = E_m \sin\left(\frac{2\pi t_{MCS}}{\Gamma_{MCS}}\right), \quad (3.16)$$

where t is the time and Γ the period. Both of them are expressed in real time. They are converted into numbers of MCS according to: $t_{MCS} = t \times (\tau_{MCS} / \tau)$ and $\Gamma_{MCS} = \Gamma \times (\tau_{MCS} / \tau)$ respectively.

With both scaled time and period derived from the thickness-dependent scaling factor according to Eqn. (3.15), the thickness dependence of coercive field in the absence of any surface effect is then simulated, plotted as the dashed curve in Fig. 3.4. It is essentially independent of thickness except when the film thickness is very small. It also reveals that in the absence of the surface effect, the experimentally observed thickness dependence cannot be reproduced. Alternatively, if we adopt a period in constant number of MCS which is not scaled according to Eqn. (3.16), the simulated thickness dependence



of coercive field will show a monotonically increasing trend, shown as the dotted curve in Fig. 3.4. For comparison purpose, the thickness dependence derived from Landau-Khalatnikov theory is also shown (solid curve). The time in Landau-Khalatnikov theory can be scaled with the viscosity coefficient [51], which is independent of thickness. The trend obtained by scaling the real period with a thickness-dependent scaling factor agrees with that obtained from Landau-Khalatnikov theory. This justifies the conversion of time by a thickness dependent scaling factor.

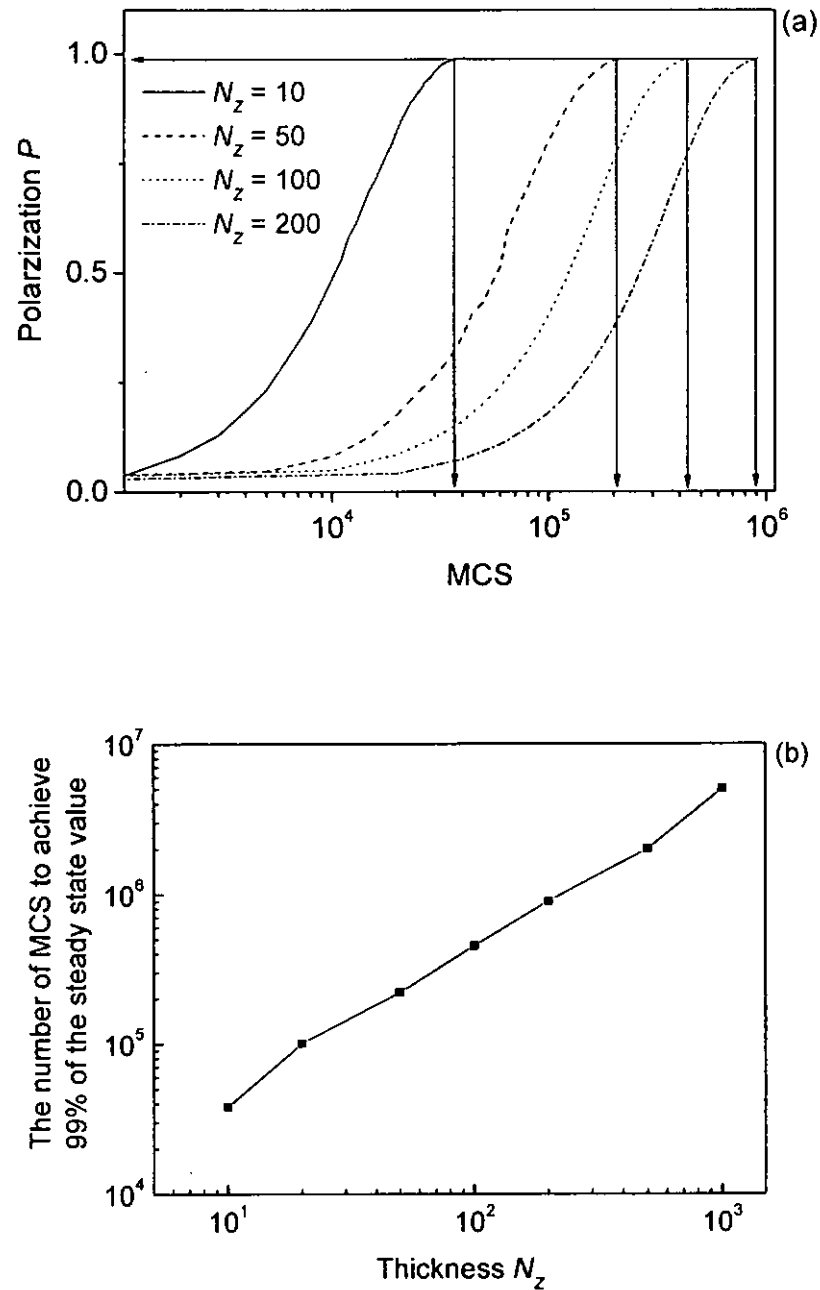


Fig. 3.3 (a) Plots of polarization against number of MCS for different thicknesses. The numbers of MCS to achieve 99% steady state value for different thicknesses are also shown. (b) Plots of the number of MCS to achieve 99% of the steady state polarization against thickness N_z . The number of MCS increases with thickness.

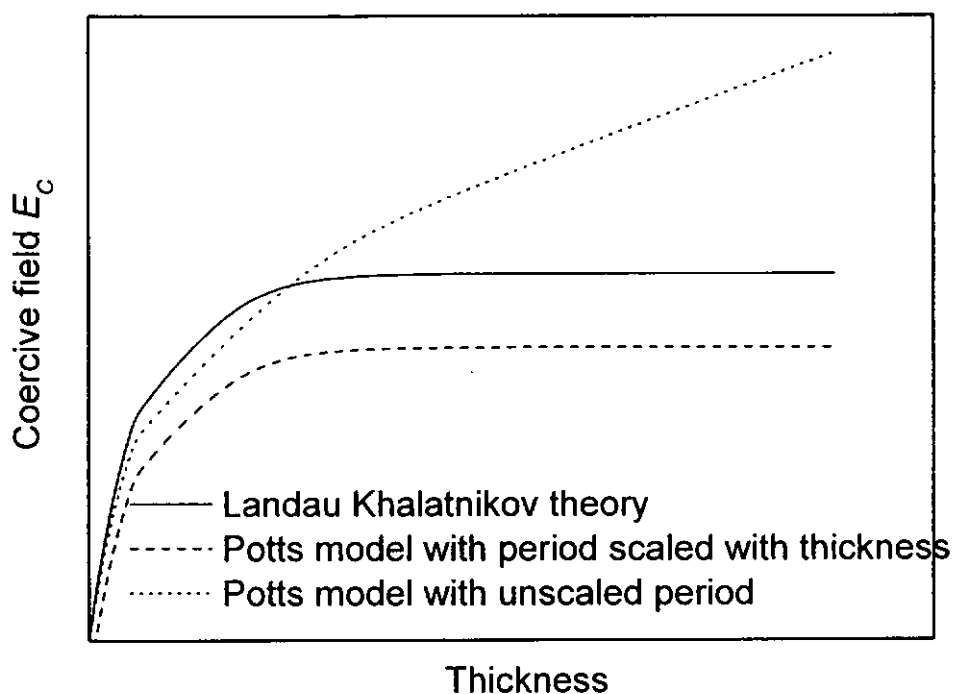


Fig. 3.4 Thickness dependence on coercive field evaluated from (i) Landau-Khalatnikov theory (solid line), (ii) Potts model period scaled with thickness (dashed line), and (iii) Potts model with unscaled period (dotted line).



3.4 Expected Simulation Results

The validity of our present model has been tested by investigating the effects of temperature, frequency and amplitude of driving electric field because experimental reports of these effects are well documented and noncontroversial. It is expected that the coercive field increases on increasing either the frequency or amplitude of the electric field, or both, but it decreases with temperature [52, 53]. In Fig. 3.5, the simulation result shows that the coercive field e_c increases on decreasing the period Γ_{MCS} . As the frequency is the reciprocal of the period, such that $f = 1/\Gamma$, the frequency dependence of coercive field obtained from our simulation qualitatively agrees with experiments. In Fig. 3.6, it shows the increase of coercive field on increasing the amplitude of the electric field. The temperature dependence of coercive field is shown in Fig. 3.7. All of them agree with experiments.

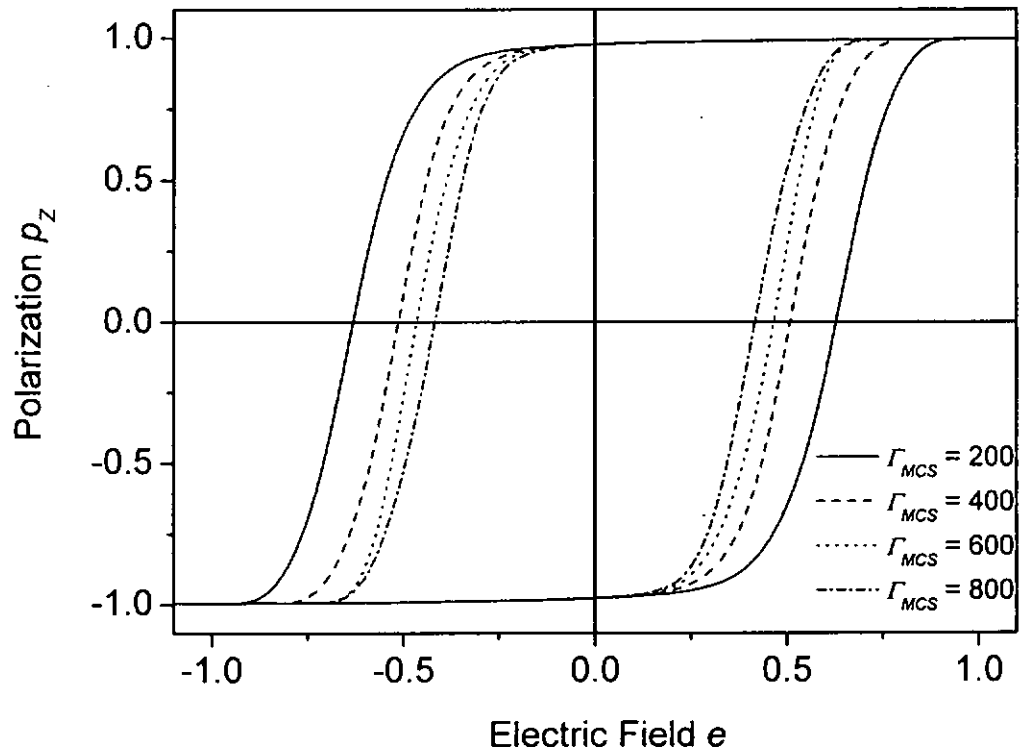


Fig. 3.5 Hysteresis loops for different values of periods: (i) $\Gamma_{MCS} = 200$ (solid line), (ii) $\Gamma_{MCS} = 400$ (dashed line), (iii) $\Gamma_{MCS} = 600$ (dotted line), and (iv) $\Gamma_{MCS} = 800$ (dash-dotted line).

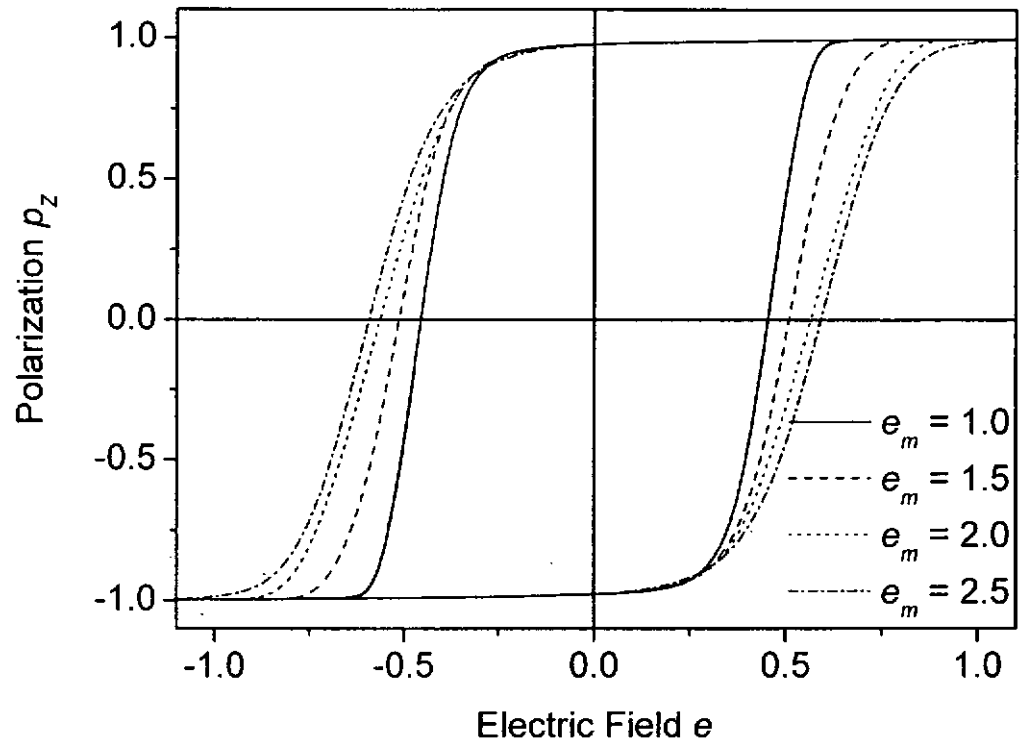


Fig. 3.6 Hysteresis loops for different amplitudes of driving electric field e_m : (i) $e_m = 1.0$ (solid line), (ii) $e_m = 1.5$ (dashed line), (iii) $e_m = 2.0$ (dotted line), and (iv) $e_m = 2.5$ (dash-dotted line).

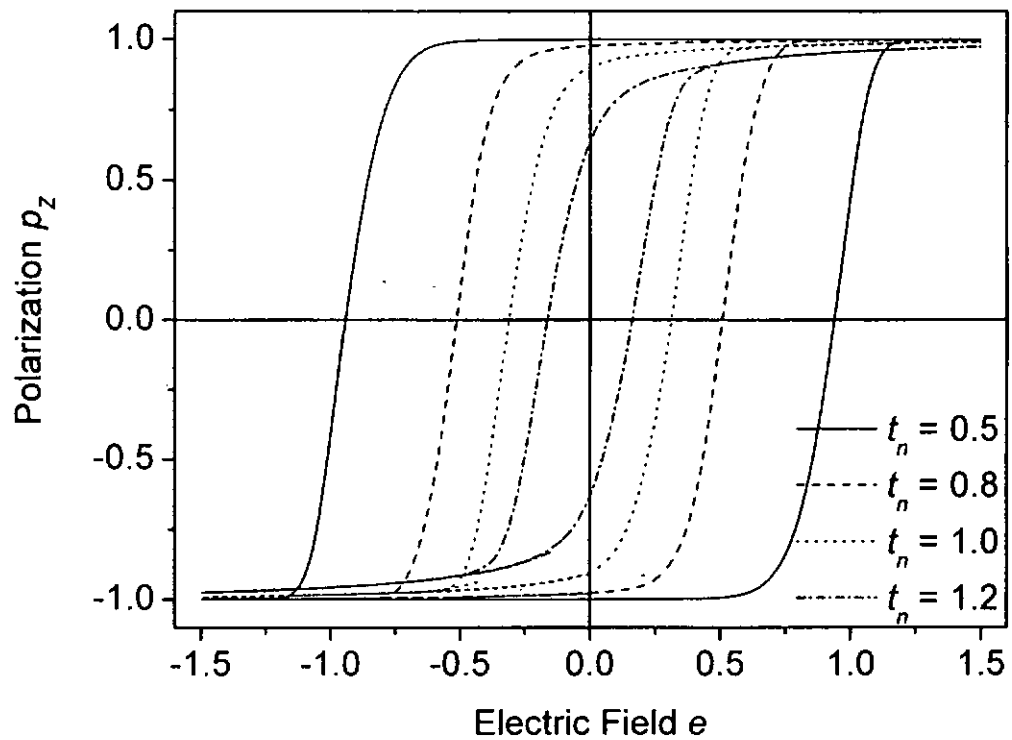


Fig. 3.7 Hysteresis loops at different temperatures (i) $t_n = 0.5$ (solid line), (ii) $t_n = 0.8$ (dashed line), (iii) $t_n = 1.0$ (dotted line), and (iv) $t_n = 1.2$ (dash-dotted line).



CHAPTER IV

SIMULATION OF THICKNESS DEPENDENCE IN THE PRESENCE OF SURFACE LAYER

4.1 Basic Assumptions

In this chapter, we have assumed that two surface layers exist at both the top and bottom electrode/film interfaces. Within a surface layer, the coupling coefficient and the dipole moment are different from those in the bulk region. In particular, the former is larger but the latter is smaller than their bulk counterparts.

This difference is attributed to the difference in tetragonality at the interfacial layer and also the presence of defects. Wang *et al.* [54] have also adopted a different coupling coefficient at the surface layer due to the different tetragonality and the presence of strain at the electrode/film interface.

In the presence of surface layers between the electrode and the thin film, the coupling coefficient $J_{i,j}$ for the dipole located at position (i, j) in the film can be expressed as

$$J_{i,j} = \begin{cases} J^S & (1 \leq j \leq N_s \text{ and } (N_z - N_s) < j \leq N_z) \\ J^B & (\text{Otherwise}) \end{cases} \quad (4.1)$$

where J^S is the surface coupling coefficient, J^B is the bulk coupling coefficient, N_s is the thickness of the surface layer in terms of number of monolayers. In Eqn. (4.1), it is



obvious that the coupling coefficient only varies along the thickness direction, acquiring two different values at the surface layer and in the bulk, respectively.

Similarly, the dipole moment at an arbitrary layer is given by

$$P_{o,i,j} = \begin{cases} P_o^S & (1 \leq j \leq N_s \text{ and } (N_z - N_s) < j \leq N_z) \\ P_o^B & (\text{Otherwise}) \end{cases} \quad (4.2)$$

The above variables are then normalized to dimensionless variables according to the following relations:

$$\begin{aligned} j_n^S &= J / J^B, \quad j_n^B = J^B / J^B = 1.0, \quad j_n^S = J^S / J^B, \\ p_o^B &= P_o / P_o^B, \quad p_o^B = P_o^B / P_o^B = 1.0, \quad p_o^S = P_o^S / P_o^B. \end{aligned} \quad (4.3)$$

After the conversion of variables, Eqn (3.11) is transformed into:

$$h = - \sum_{i,j,k,m} j_{n,i,j} \{ \hat{S}_{i,j}^T \hat{S}_{k,m} \} - \sum_{i,j} p_{o,i,j} \{ \hat{e}_j^T \hat{S}_{i,j} \}. \quad (4.4)$$

4.2 Simulation Results and Discussion

The resultant Polarization-Electric field (PE) loops for different thicknesses are shown in Fig. 4.1. In our present work, the following parameters were chosen: $T = 300\text{K}$, $E_m = 800\text{kV/cm}$, $J^B = 5.175 \times 10^{-21}\text{ Joules}$, $P_o^B = 3.2 \times 10^{-29}\text{ Cm}$, and $\Delta z = 0.4\text{nm}$. They were then transformed into dimensionless parameters based on the relations in Eqns. (3.10) and (4.3), yielding $t_n = 0.8$, $e_m = 0.5$, $N_s = 30$, $j_n^B = 1.0$, $j_n^S = 1.2$, $p_o^B = 1.0$, $p_o^S = 0.7$. The hysteresis loops for different thicknesses are shown in Fig 4.1. In our previous work, the thickness dependence of coercive field and remanent polarization

have been determined from these loops [55]. The results will be shown and discussed in the following paragraphs.

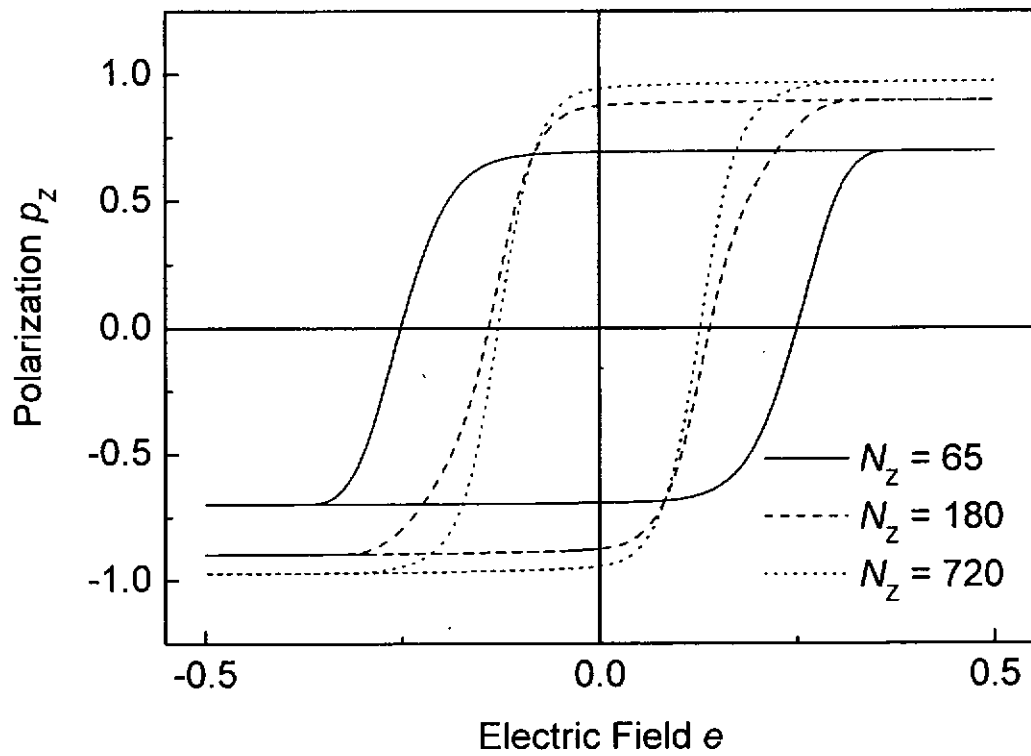


Fig. 4.1 Hysteresis loops for difference thicknesses: $N_z = 65$ (solid line), $N_z = 180$ (dashed line), $N_z = 720$ (dotted line). The parameters are: $j_n^S = 1.2$, $p_o^S = 0.7$, $j_n^B = 1.0$, $p_o^B = 1.0$, $t_n = 0.8$, $e_m = 0.5$, $N_s = 30$.



The plots of coercive field e_c against thickness N_z for different surface coupling coefficients j_n^s are shown in Fig. 4.2. It reveals that coercive field increases monotonically with thickness when $j_n^s = 1.0$, which is simply the case without the surface effect. When $j_n^s > 1.0$, two different trends appear in the thickness dependence curve. For $N_z < 60$, e_c increases with N_z , and for $N_z > 60$, e_c decreases on increasing the film thickness until it approaches an asymptotic value for a very large N_z . The latter trend agrees with experiments [9-12]. For $N_z < 60$, the film becomes a one-layer system such that the film properties are completely determined by the “surface” layer. The monotonically increasing trend for coercive field thus appears.

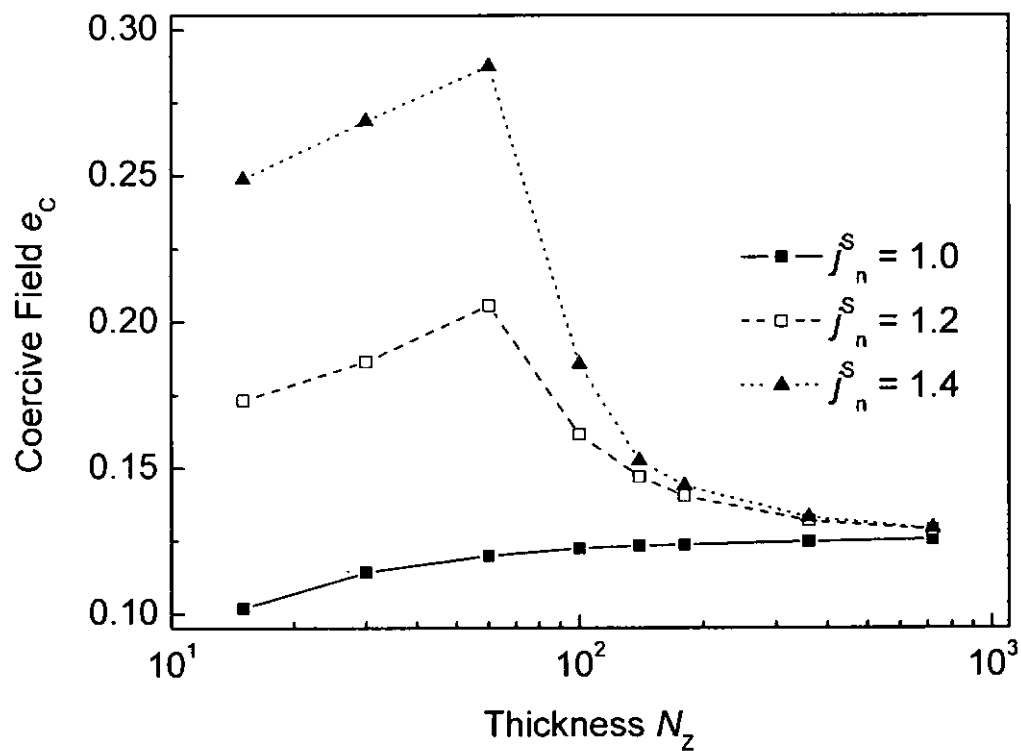


Fig. 4.2 Thickness dependence of coercive field for different surface coupling coefficients. The surface dipole moment is set equal to the bulk dipole moment ($p_o^B = 1.0$). Other parameters are the same as in Fig. 4.1.

The thickness dependence of remanent polarization p_r for different values of surface dipole moment p_o^S is shown in Fig. 4.3. It reveals that the increasing trends of remanent polarization can only be reproduced when $p_o^S < 1$. Similarly, the remanent polarization also approaches an asymptotic value when the thickness N_z is large enough.

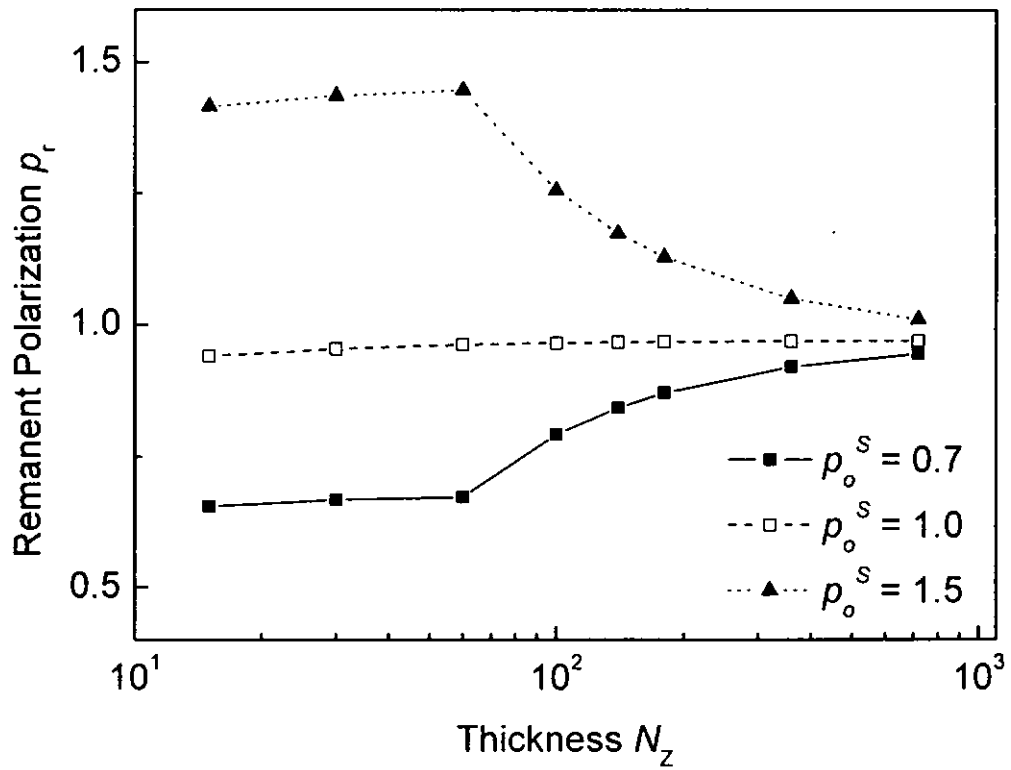


Fig. 4.3 Thickness dependence of remanent polarization for different surface dipole moments. The surface coupling coefficient is set equal to the bulk coupling coefficient ($j_n^B = 1.0$). Other parameters are the same as in Fig. 4.1.

The polarization profiles at $1/4$ and $3/4$ of a cycle are shown in Fig. 4.4. It reveals that the surface layer is still ferroelectric: switchable but with a depressed polarization value. Such a depression in surface polarization might be attributed to the smaller c/a ratio at the surface, as observed from experiment [56]. Similar result has been obtained by Baudry *et al.* [22] in the presence of depolarizing field at the interface.

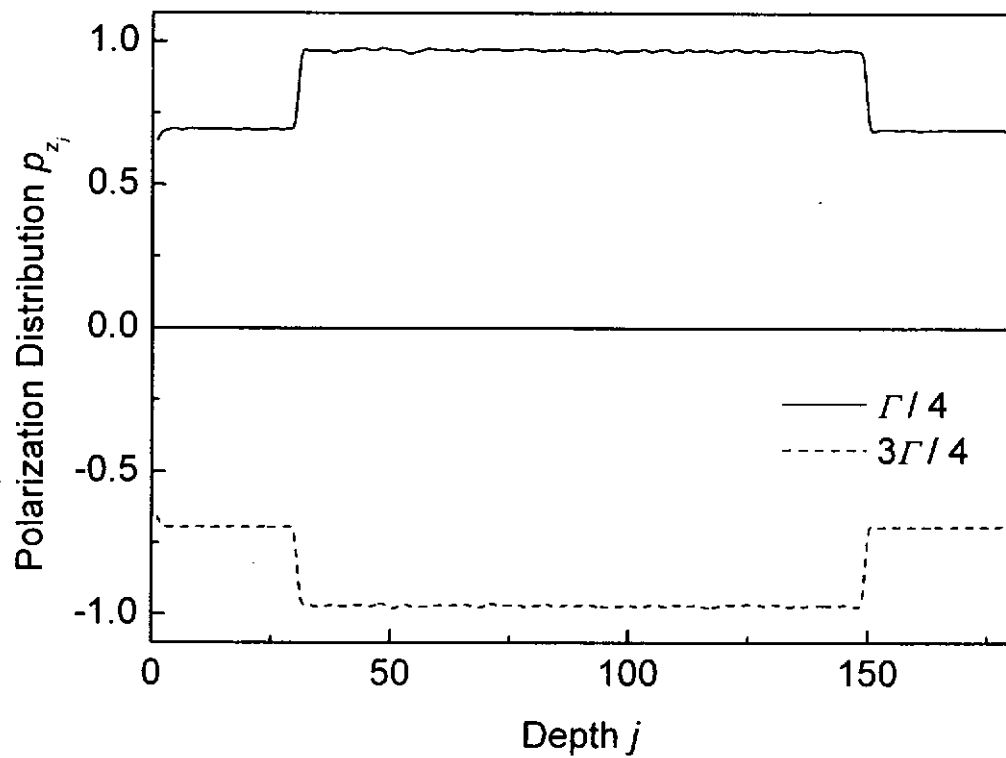


Fig. 4.4 Polarization profiles across the film of thickness $N_z = 180$ at different times: one-quarter (solid line) and three-quarter (dashed line). The parameters are the same as in Fig. 4.1.

PE loops at different layers (top, bottom and middle) of the film together with the overall loop of the whole film are shown in Fig. 4.5. By comparing the PE loops in the surface layer and in the internal region, the coercive field e_c of the surface layer is much larger but the remanent polarization p_r is much smaller than their counterparts in the internal region.

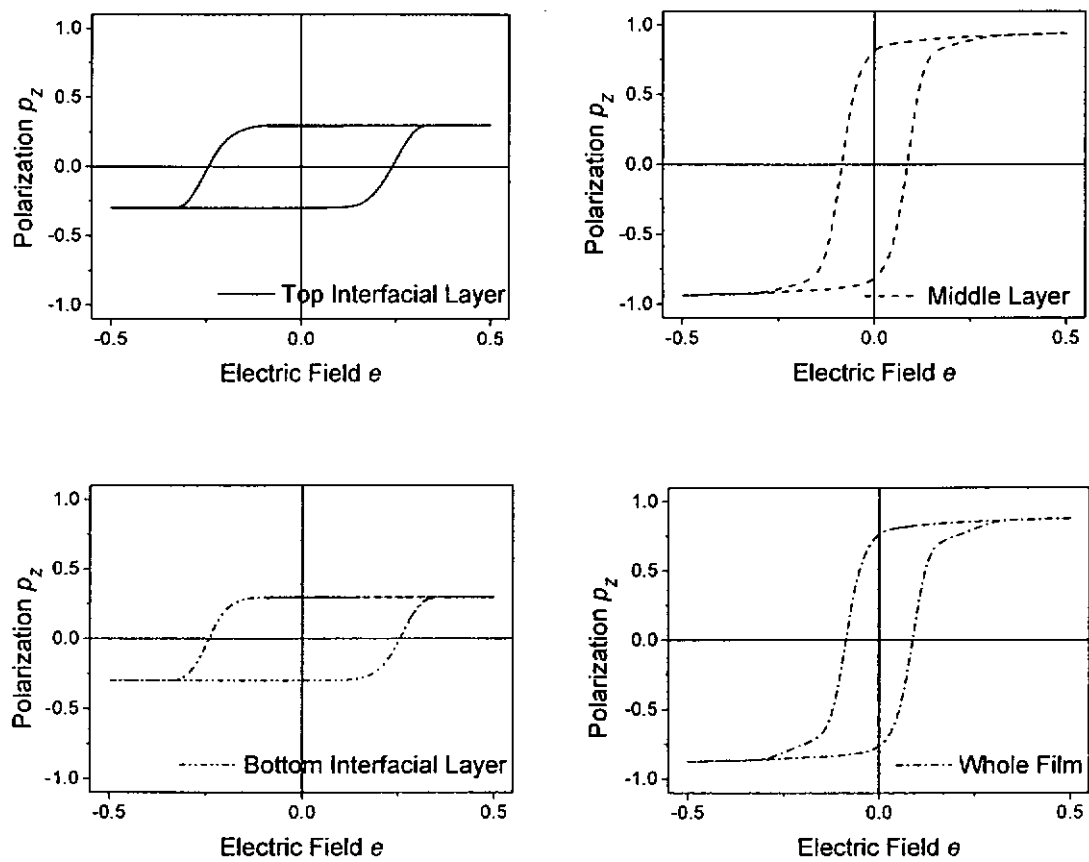


Fig. 4.5 P-E loops at the (a) top interfacial layers, (b) middle layer, (c) bottom interfacial layer. Overall P-E loop for the whole film is shown in (d).



Besides the difference in material parameters in the presence of the surface layer, the presence of space charge and depolarizing field at the surface layer might also contribute some effects on the thickness dependence. They are either induced by point defects at the electrode/film interface, or resulted from the incomplete compensation of charge by the electrode.

A space charge layer of a thickness d_{sc} can exist beneath the electrode/film interface. In this layer, free charge carriers such as electrons and holes, are depleted. Moreover, it has been shown before that the polarization profile along the film thickness is essentially uniform except at the electrode/film interface. For simplicity, it is assumed that total charge density inside the space charge layer is uniformly distributed with a charge density ρ_o . The induced local field E_{sc} can be obtained by solving the Poisson equation:

$$\frac{dE_{sc}}{dz} = \frac{\rho_o}{\epsilon_r \epsilon_o}, \quad (4.5)$$

where ϵ_r is the relative dielectric permittivity and ϵ_o is the dielectric permittivity of vacuum. Superimposing the induced local field into the external driving field e_{ext} across the film, the total normalized electric field at an arbitrary layer j is given by

$$e_j = e_{ext} + e_{sc}$$
$$e_j = \begin{cases} e_{ext} + (j - N_{sc})\rho_{on} & (1 \leq j \leq N_{sc}) \\ e_{ext} + [j - (N_z - N_{sc})]\rho_{on} & ((N_z - N_{sc}) < j \leq N_z), \\ e_{ext} & (\text{Otherwise}) \end{cases} \quad (4.6)$$



where $\rho_{on} = \rho_o P_o^B \Delta z / (\epsilon_r \epsilon_o J^B)$, $d_{sc} = N_{sc} \Delta z$ and $d = N_z \Delta z$.

The effect of space charge on the thickness dependence of coercive field e_c is shown in Fig. 4.6(a), and (b) for $j_n^S = 1.0$ and $j_n^S = 1.2$ respectively. From Fig. 4.6(a), in the absence of the surface layer so that the difference in material parameters disappears, all trends are monotonically increasing. Thus, the presence of space charge can not explain the decreasing trend of the coercive field. In the presence of surface layer with space charge, we would expect that a decreasing trend of coercive field is reproduced for large thickness. However, In Fig. 4.6(b), the decreasing trend for large thickness is only the consequence of adapting different parameters for the surface layer. Moreover, this decreasing trend is disappears when ρ_{on} is large. It clearly demonstrates that the presence of space charge does not lead to the expected decreasing trend.



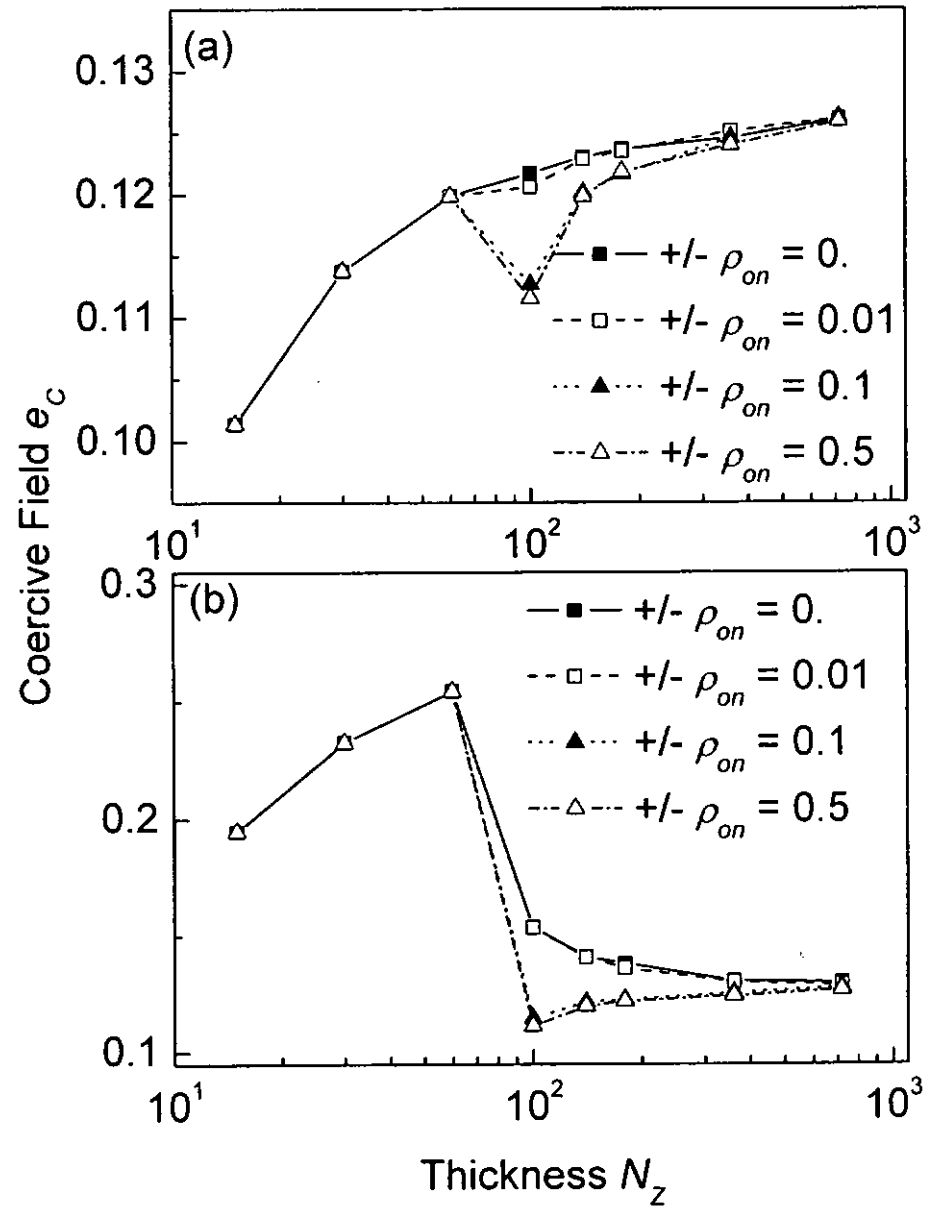


Fig. 4.6 Effect of space charge on the thickness dependence of coercive field (a) $j_n^S = 1.0$ and (b) $j_n^B = 1.2$ with different ρ_{on} values, all other parameters except j_n^S are the same as in Fig. 4.1.

Due to the inhomogeneity in polarization or incomplete compensation of polarization charge, a depolarization field is present at the surface layer within a thickness d_{dep} . The depolarization field [57] can be related by

$$E_{dep} = -\gamma P, \quad (4.7)$$

where γ is the depolarizing factor depending on both on the geometry and the charge compensation at the electrode. Typically, the polarization is homogeneous inside the film and non-uniform in the surface layer. The depolarizing field thus only exists at the surface layer. The total normalized electric field at an arbitrary j^{th} layer can be expressed by

$$e_j = \begin{cases} e_{ext} - \gamma_n p_j & (1 \leq j \leq N_{dep} \text{ and } (N_z - N_{dep}) < j \leq N_z) \\ e_{ext} & (\text{Otherwise}) \end{cases} \quad (4.8)$$

where p_j is the average polarization at the j^{th} layer, $\gamma_n = \gamma(P_o^B)^2 / (J^B)$, $d_{dep} = N_{dep} \Delta z$ and $d = N_z \Delta z$.

The effect of depolarization on the thickness dependence of coercive field e_c is shown in Figs. 4.7(a) and (b) for $j_n^S = 1.0$ and $j_n^S = 1.2$, respectively. In Fig. 4.7(a), in the absence of the surface layer, all trends are monotonically increasing. Consequently, the presence of the depolarizing field also cannot explain the decreasing trend of the coercive field. In Fig. 4.7(b), a decreasing trend is obtained for large thickness, in the presence of the surface layer.

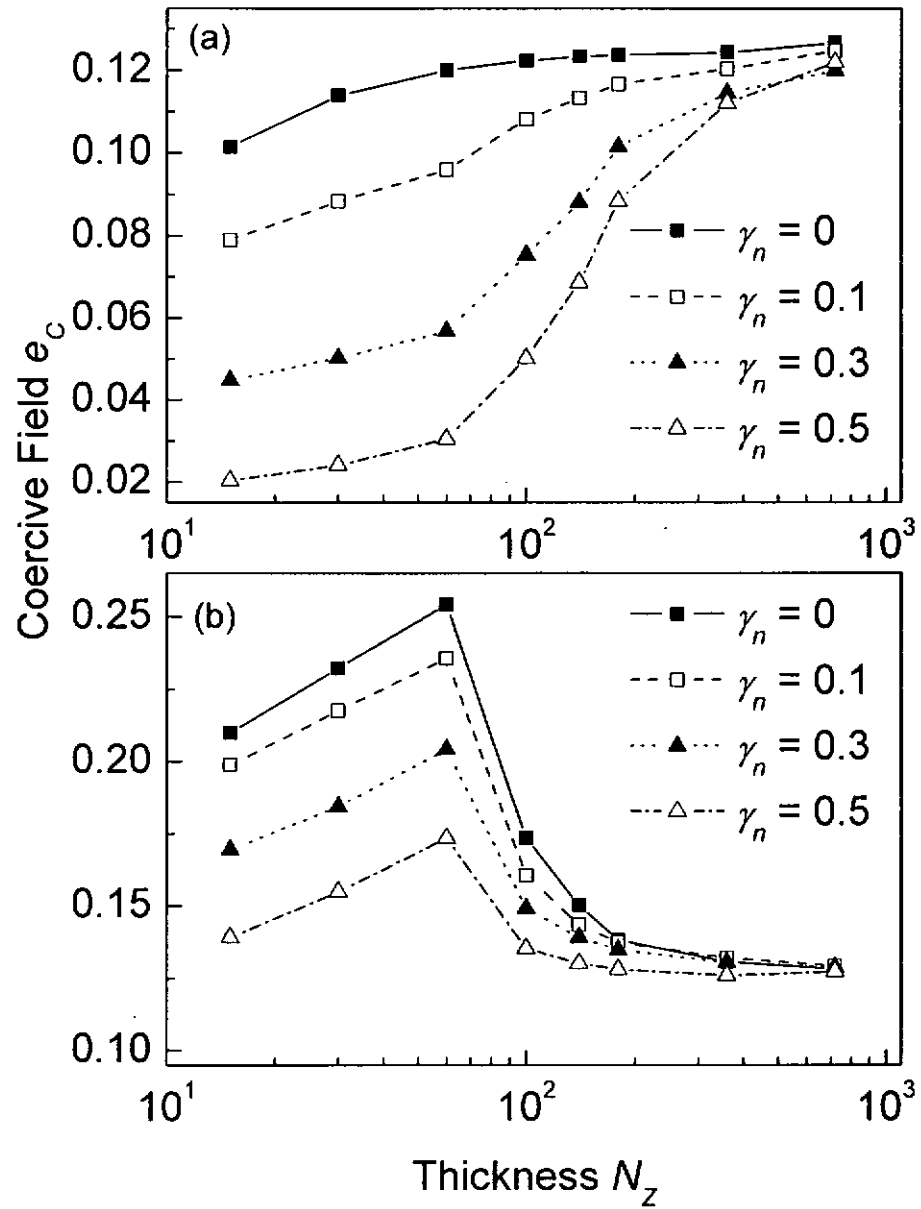


Fig. 4.7 Effect of depolarization on the thickness dependence of coercive field (a) $j_n^S = 1.0$ and (b) $j_n^B = 1.2$ with different γ_n values, all other parameters except j_n^S are the same as in Fig. 4.1.



Thickness dependence of coercive field has been extensively studied and attributed to the presence of interfacial layer [20, 21]. In particular, many authors considered the interfacial layer to be non-ferroelectric with a thickness of a few nanometers [22]. However, experiments revealed that ferroelectricity could still exist in films of a few nanometers thick [58]. Thus the assumption of a non-ferroelectric interfacial may not be accurate. In our present work, instead of assuming of a non-ferroelectric layer, we propose that this layer is still ferroelectric and with a larger coupling coefficient in the surface region than in the bulk region.

The effects of space charge and depolarizing field on thickness dependence of coercive field have been discussed before. Lo [25] has discussed the effects of space charge and depolarizing field on the thickness dependence of coercive field using Landau-Khalatnikov theory. His result reveals that both space charge and depolarizing field are not the primary reasons for the decreasing trend of the thickness dependence of coercive field, especially for large thickness. On the other hand, Baudry *et al.* [22] have simulated the thickness dependence of coercive field using Landau-Devonshire theory. They have a similar conclusion on the depolarization field. The present simulation result on the effects of depolarizing field and space charge agree with the conclusion drawn before: both of them are not the primary cause for the thickness dependence of coercive field.

In addition to the assumption of a step-wise distribution for the coupling coefficient over the film thickness, it is more realistic to consider a smoothly varying distribution. In fact, in the next chapter, we have investigated the effect of a gradually



distributed oxygen vacancy concentration on the coercive field and remanent polarization. The oxygen vacancy concentration was found to be closely related with the coupling coefficient. Consequently, the coupling coefficient should also be smoothly varying over the film thickness. It is expected to yield better fitting for experimental results.



CHAPTER V

PHENOMENA IN FERROELECTRIC THIN FILMS

IN THE PRESENCE OF OXYGEN VACANCIES

5.1 The Role of the Oxygen Vacancy on the Switching of Dipole

As discussed in chapter III, we consider only four possible locations for oxygen vacancy in a cell for simplicity. Likewise, the three dimensional tetragonal cell can be simplified by a rectangle lying in the XZ plane. Moreover, it is assumed that the number of vacancies in the film is dilute enough that there can be at most only one vacancy in a cell. There are two different types of domains: c – domains and a – domains. For the first type, the elongated axis is along the thickness direction (or z – axis). For the second type, the elongated axis is along the transverse direction (or x – axis). For a cell inside a c – domain, there are two off-centre equilibrium positions above and below of the centre of the rectangle. In the absence of oxygen vacancy, Ti^{4+} ion is located at one of these equilibrium positions with equal probability. The potential profile along z – axis is symmetric. For a cell inside an a – domain, these two equilibrium positions are located at the left and right of the centre. The cells inside the domain wall are distorted, there might be four equilibrium positions in a distorted rectangle, two above or below the centre with displacement along the z – axis and the other two at the left and right side of the centre by displacing along the x – axis. In the presence of an oxygen vacancy at the top plane of the cell, because of the imbalance in Coulombic interactions between ions and the distortion of the otherwise symmetric rectangle, the potential energy for the Ti^{4+} ion is



lowest at the bottom equilibrium position. Correspondingly, the potential energy at the top equilibrium position must be highest [8]. The potential energies of the two equilibrium positions at the left or right of the centre are intermediate. An additional energy say $2H_{p1}$, is required for the Ti^{4+} ion to displace from the bottom equilibrium position to the top one. Conversely, the same amount of energy is released through the reverse displacement. The expense in energy for the displacement of Ti^{4+} ion from the bottom to the left or right equilibrium position, is H_{p1} . If the dipole switching is restricted to only 90° , the Ti^{4+} ion originally located at the bottom equilibrium position will displace to either the left or right equilibrium position instead of the top one. For an unstrained rectangle deep inside the domain, there are only two possible equilibrium positions, only 180° dipole switching takes place. Rectangles inside 90° domain wall are highly strained that four off-centre equilibrium positions exist, enabling 90° dipole switching. It was found from experiments that 90° switching expense less energy so that this mechanism is dominant. Consequently, dipole switching usually takes place at the domain wall. This can be visualized as the domain wall movement. The 180° switching can be treated as the combination of two consecutive 90° switching. The energy exchange through 90° dipole switching is summarized in Fig. 5.1. The switching directions of dipole can be opposite to those shown in Fig. 5.1, with energy exchanges equal in magnitudes but opposite in signs. Moreover, the position of the oxygen vacancy can be at other positions of the cell. The same relative position of Ti^{4+} ion with respect to the oxygen vacancy results in the same potential energy.

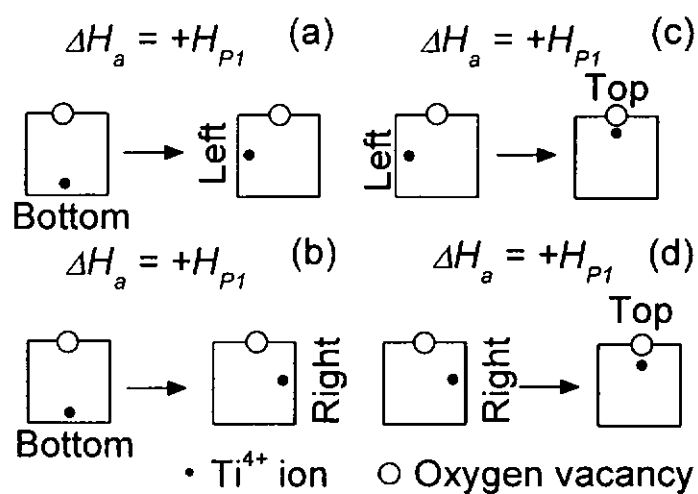


Fig. 5.1

In the presence of the oxygen vacancy at the top plane, an additional energy H_{p1} is required to displace Ti^{4+} ion from and to the following equilibrium positions: (a) from the bottom to left, (b) bottom to right, (c) left to top, and (d) right to top.

5.2 Mathematical Representation of an Oxygen Vacancy in a Cell

In our model, the presence of an oxygen vacancy in a rectangle cell specified by a pair of indices (i, j) can be represented by the state matrix $\hat{V}_{i,j}$, with the following values to represent its different locations in the cell:

$$\hat{V}_{i,j} = \begin{cases} \begin{bmatrix} 0 \\ 0 \end{bmatrix} & \text{(Vacancy is absent),} \\ \begin{bmatrix} 0 \\ 1 \end{bmatrix} & \text{(at the left plane),} \\ \begin{bmatrix} 0 \\ -1 \end{bmatrix} & \text{(at the right plane).} \end{cases} \quad \begin{cases} \begin{bmatrix} 1 \\ 0 \end{bmatrix} & \text{(at the top plane),} \\ \begin{bmatrix} -1 \\ 0 \end{bmatrix} & \text{(at the bottom plane),} \end{cases} \quad (5.1)$$

Oxygen vacancies are generated from outside, diffusing into the film through the electrodes. The distribution of oxygen vacancies across the thickness of the film can be expressed by the following function:

$$f(z) = \alpha [\exp(-z/L_{z1}) + \exp(-(d-z)/L_{z2})], \quad (5.2)$$

where L_{z1} and L_{z2} are the characteristic diffusion lengths at the top and bottom electrodes, respectively. The parameter α is a normalization constant given by

$$\alpha = \frac{1}{L_{z1}[1 - \exp(-d/L_{z1})] + L_{z2}[1 - \exp(-d/L_{z2})]}. \quad (5.3)$$

The integration of the distribution function is equal to one such that $\int_0^d f(z)dz = 1$, ensuring the same quantity of oxygen vacancies for different L_{z1} or L_{z2} values. It is also interesting to note that for uniform distribution along the z -direction, $f(z) \rightarrow 1/N_z$ as $L_{z1} = L_{z2} \rightarrow \infty$. On the other hand, oxygen vacancies are uniformly distributed along the



transverse direction. If the total number of oxygen vacancies in the film is denoted by N_v , then the number along a transverse monolayer at a distance z from the top surface is given by $n(z) = N_v f(z)$. The probability that a vacancy exists in a cell located at (i, j) position is given by $r(x, z) = n(z) / N_x = N_v f(z) / N_x$.

5.3 Space Charge Released by Oxygen Vacancy

An oxygen vacancy can trap holes or release electron to become a positive space charge [35]. Under thermal equilibrium, the number of charged vacancies N_v^+ depends on both the position of Fermi level E_F and temperature T , as expressed by the following relation [59]

$$N_v = N_v^x + N_v^+, \quad (5.4)$$

where

$$N_v^+ = \frac{N_v}{1 + g_A \exp\left(\frac{E_F - E_T}{kT}\right)}, \quad (5.5)$$

N_v^x is the number of neutral vacancies without trapping holes, N_v the total number of vacancies, g_A the degeneracy factor and E_T the energy of trapping level above the valence band. The local charge density ρ_{sc} is then related to N_v^+ by

$$\rho_{sc} = \frac{qN_v^+}{N_x(\Delta z)} f(z) = q_r f(z), \quad (5.6)$$

where the parameter q_r depends not only on position of Fermi level and temperature, but also on the imbalance of trapping and emission rates of charge carriers and frequency of



the alternating driving field. The charge induced local field E_{SC} can then be obtained from the Poisson equation

$$\frac{dE_{SC}}{dz} = \frac{1}{\epsilon_s \epsilon_o} \rho_{SC}. \quad (5.7)$$

If the explicit form of the distribution function is given, the analytical form for E_{SC} can be derived.

5.4 System Hamiltonian in the Presence of Oxygen Vacancies

As discussed in section 5.1, in the presence of oxygen vacancies in the ferroelectric thin film, an additional energy H_{P1} is required to displace Ti^{4+} ion from one equilibrium position to the other. In our model, this mechanism gives rise to an additional term in the system Hamiltonian as follows:

$$H_a = \sum_{i,j} H_{P1} \{\hat{V}_{i,j}^T \hat{S}_{i,j}\}. \quad (5.8)$$

Moreover, the presence of an oxygen vacancy in a perovskite cell also induces distortion to this cell. This distortion influences the coupling with the neighboring dipoles. Thus another additional contribution H_b must be included, where

$$H_b = -H_{P2} \sum_{i,j,k,m} \{\hat{V}_{i,j}^T \hat{V}_{i,j}\} \{\hat{S}_{i,j}^T \hat{S}_{k,m}\}. \quad (5.9)$$

The system Hamiltonian now becomes

$$H = H_o + H_a + H_b, \quad (5.10)$$

where H_o is the Hamiltonian in the absence of oxygen vacancies, as given by Eqn. (3.8).



The above variables are converted into dimensionless forms by the following relations:

$$\begin{aligned}
 h_{p1} &= H_{p1} / J^B, & h_{p2} &= H_{p2} / J^B, \\
 N_{z1} &= L_{z1} / \Delta z, & N_{z2} &= L_{z2} / \Delta z, \\
 q_m &= \frac{P_o^B q N_v^+}{J^B \epsilon_s \epsilon_o N_x (\Delta z)^2}, & f_n(j) &= \frac{f(z)}{\Delta z}, \\
 e_{sc}(j) &= q_m \int_0^j f_n(j') dj'. \tag{5.11}
 \end{aligned}$$

The electric field matrix, including both external driving field and the charge induced local field, now becomes,

$$\hat{e} = \begin{bmatrix} e_{ext} + e_{sc} \\ 0 \end{bmatrix}, \tag{5.12}$$

After the conversion, the normalized Hamiltonian now becomes

$$h = - \sum_{i,j,k,m} \{ \hat{S}_{i,j}^T \hat{S}_{k,m} \} - \sum_{i,j} \{ \hat{e}_j^T \hat{S}_{i,j} \} + h_{p1} \sum_{i,j} \{ \hat{V}_{i,j}^T \hat{S}_{i,j} \} - h_{p2} \sum_{i,j,k,m} \{ \hat{V}_{i,j}^T \hat{V}_{i,j} \} \{ \hat{S}_{i,j}^T \hat{S}_{k,m} \}. \tag{5.13}$$

5.5 Simulation Results on the Thickness Dependence

We have simulated the hysteresis loops using the following parameters:

$$J^B = 5.175 \times 10^{-21} \text{ Joules}, \quad P_o^B = 3.2 \times 10^{-29} \text{ Cm}, \quad T = 300 \text{ K}, \quad E_m = 800 \text{ kV/cm},$$

$\Delta z = 0.4 \text{ nm}$, $H_{p1} = 1.035 \times 10^{-20} \text{ Joules}$, and $H_{p2} = 3.105 \times 10^{-20} \text{ Joules}$. By the relations in Eqns. (3.10), (4.3) and (5.11), we have the following normalized parameters: $t_n = 0.8$,



$e_m = 0.5$, $N_x = 2048$, $N_z = 100$, $h_{p1} = 2.0$, $h_{p2} = 6.0$. Moreover, based on Eqn (5.2) and (5.11), the oxygen vacancy distribution function, which is fixed in time, can be determined by the following parameters: $N_v = 60000$, $N_{z1} = 30$, $N_{z2} = 30$. In our present work, each cell can only consist of one oxygen vacancy, such that the total number of oxygen vacancies N_v must be smaller than the sample size ($N_x N_z$). The resultant Polarization-Electric (PE) hysteresis loops for different thicknesses are shown in Fig. 5.2.

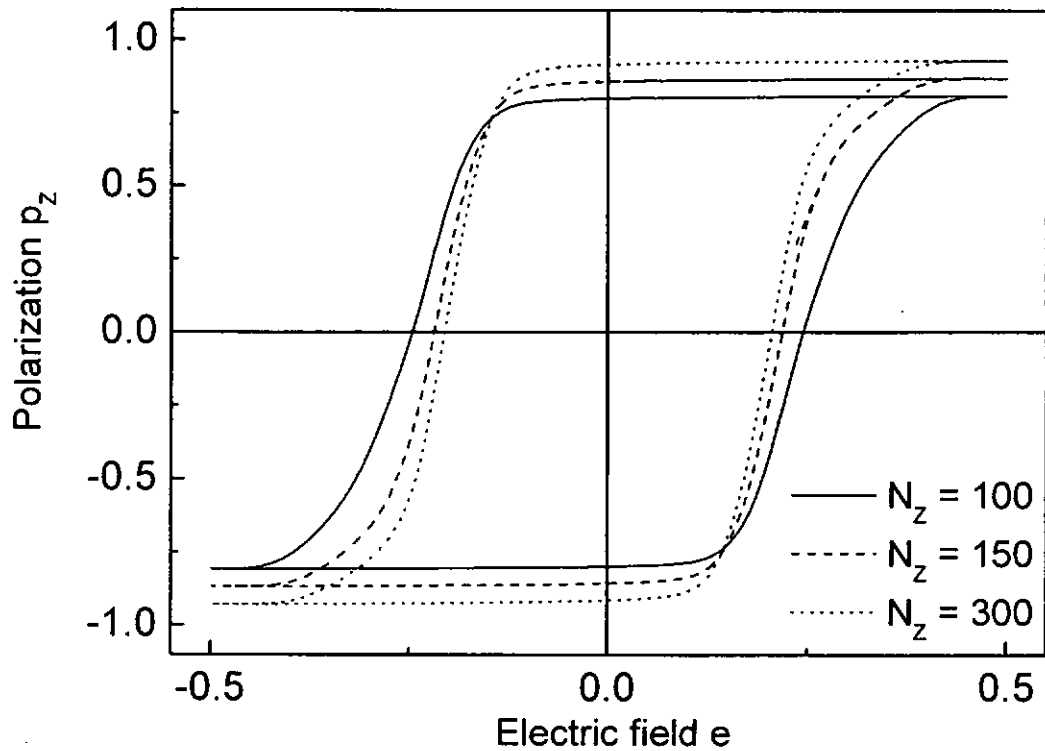


Fig. 5.2 Hysteresis loops for difference thicknesses: $N_z = 100$ (solid line), $N_z = 150$ (dashed line), $N_z = 300$ (dotted line). Other parameters are listed in the text.

The corresponding thickness-dependence of coercive field for different number of oxygen vacancies N_V is shown in Fig. 5.3. It reveals that the coercive field e_c monotonically decreases on increasing thickness until it approaches an asymptotic value for large thickness N_Z . Moreover, the slope for a fixed N_Z increases with N_V .

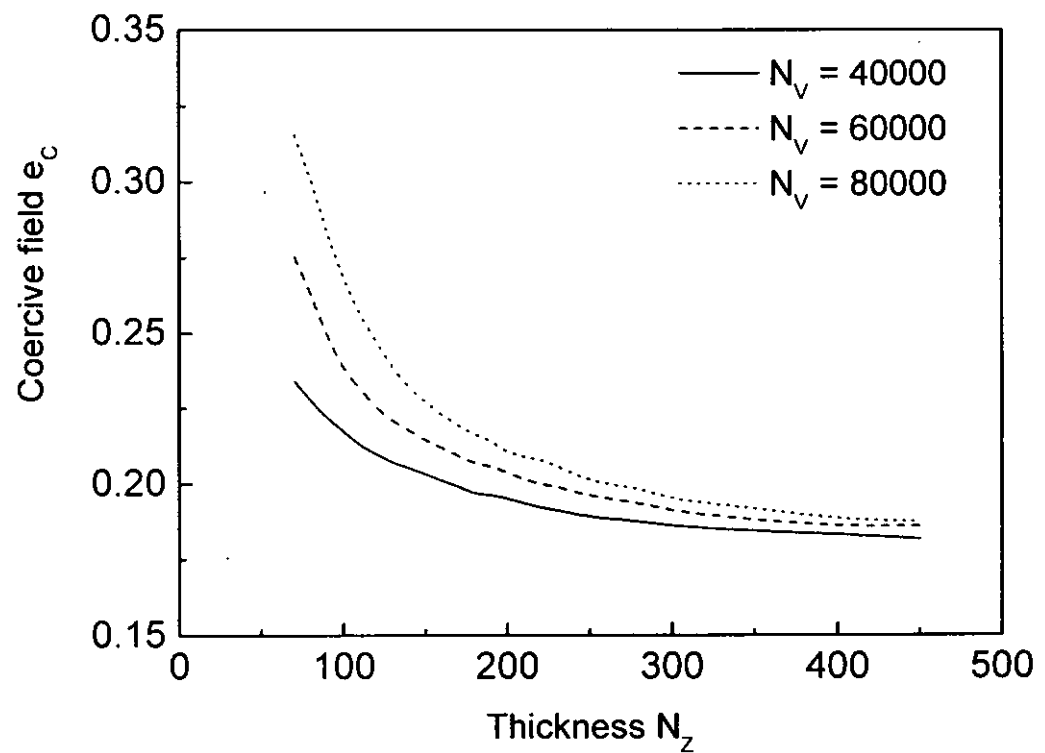


Fig. 5.3 Thickness dependence of coercive field e_c for different number of oxygen vacancies N_V .

The thickness dependence of remanent polarization p_r is shown in Fig. 5.4. Similar to the numerous experimental results [9-12], the remanent polarization increases with thickness. Moreover, the reduction of remanent polarization is pronounced in the presence of oxygen vacancies.

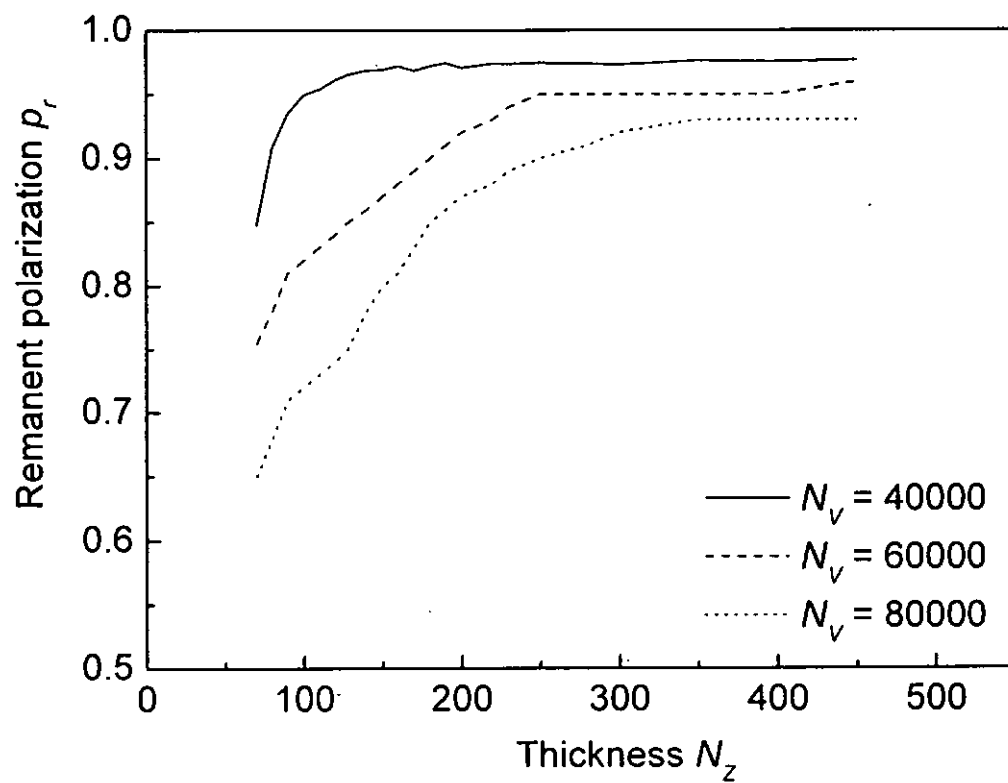


Fig. 5.4 Thickness dependence of remanent polarization p_r for different number of oxygen vacancies N_v .

Using our present model, we have fitted the experimental result of Fujisawa *et al.*'s [9], as shown in Fig. 5.5 for the coercive field E_c and Fig. 5.6 for the remanent polarization P_r , respectively. The fitting parameters are as follows: $P_o^B = 2.944 \times 10^{-29} \text{ Cm}$, $J^B = 4.14 \times 10^{-21} \text{ Joules}$, $E_m = 400 \text{ kV/cm}$, $T = 300 \text{ K}$, $L_{z1} = L_{z2} = 7.5 \text{ nm}$, $\Delta z = 0.4 \text{ nm}$, $N_v = 1 \times 10^5$.

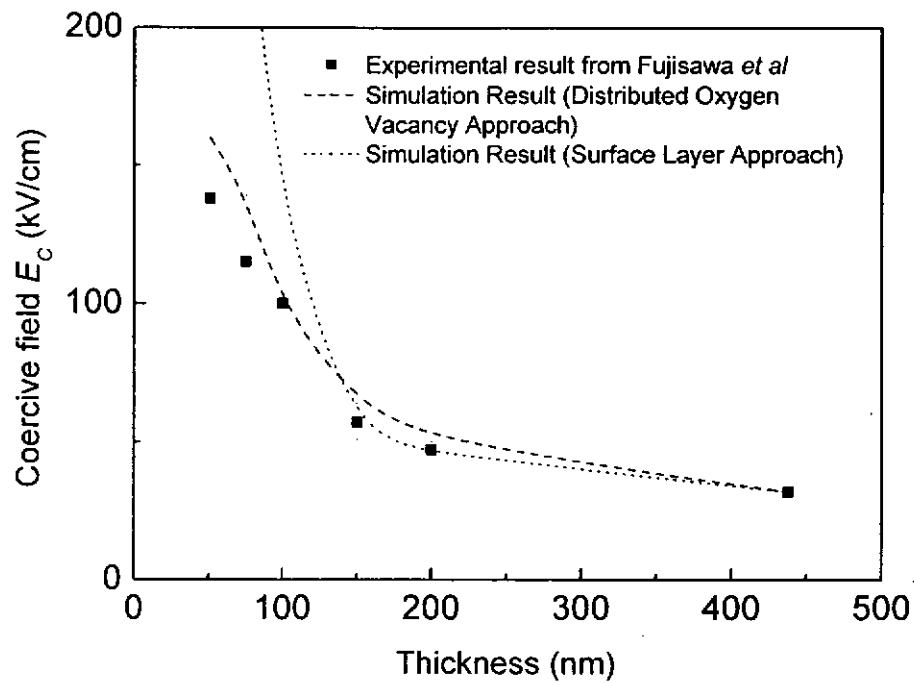


Fig. 5.5 Thickness dependence of coercive field E_c from (i) experimental result of Fujisawa *et al.* [9] (solid squares), (ii) simulation result in the presence of oxygen vacancies (dashed line), and (iii) simulation result in the presence of surface layer (dotted line).

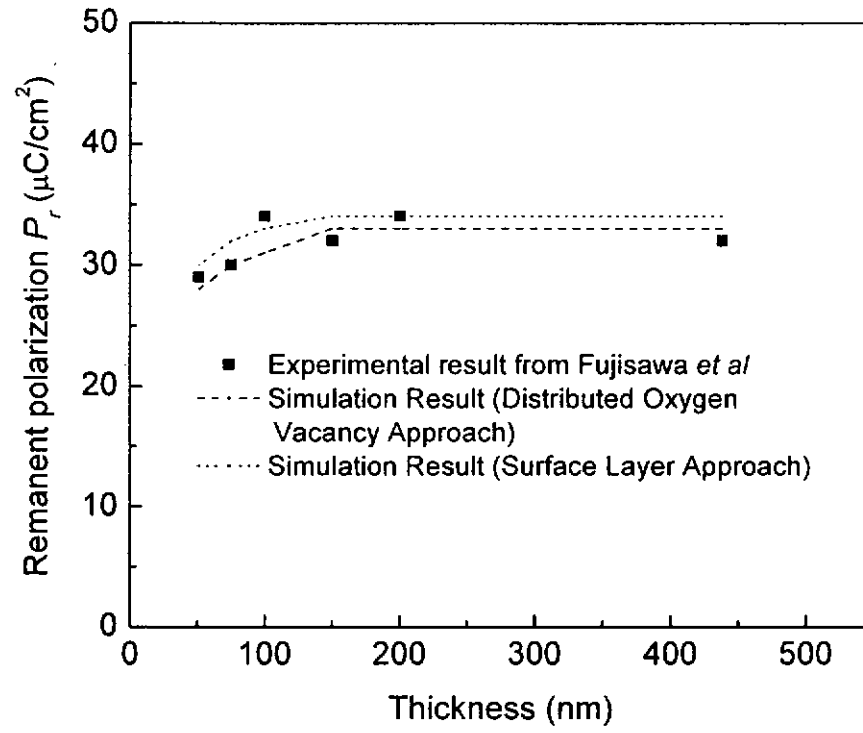


Fig. 5.6 Thickness dependence of remanent polarization P_r from (i) experimental result from Fujisawa *et al.* [9] (solid squares), (ii) simulation result in the presence of oxygen vacancies (dashed line), and (iii) simulation result in the presence of surface layer (dotted line).



In Figs. 5.5 and 5.6, the simulation results in the presence of oxygen vacancies are plotted as dashed curves. The experimental results are in solid squares. Comparing our curves with the experimental result, the fitting is quite good except a slight deviation at small thickness. On one hand, it is related to the fine-tuning of fitting parameters. On the other, the coercive field E_C is usually obtained from dividing the coercive voltage V_C by the thickness d , so that $E_C = V_C / d$. For small thickness, a significant error in ΔE_C results because a large relative error in thickness measurement $\Delta d / d$ leads to a large relative error in coercive field through the relation $\Delta E_C / E_C \sim \Delta d / d$.

Furthermore, the simulation results by assuming the presence of surface layer with different coupling coefficients are also shown in the same figures (as dotted curves). Comparing the simulation results using both approaches, they both agree with experiments quite well for large thickness. However, for small thickness, the simulation result derived from the surface-layer approach has quite a significant deviation from experiment. The simulation result derived from the distributed oxygen-vacancy approach yields better fitting. Two conclusions can be drawn. Firstly, the presence of oxygen vacancies equivalently enhanced the coupling coefficient. In Fig. 5.7, a linear relation between the number of vacancies in the film N_v and the coupling coefficient j_n^S is shown. This relation was obtained from the simulation of the thickness dependence of coercive field from these two approaches. The surface coupling coefficient j_n^S based on the surface layer approach and the number of vacancies N_v based on the distributed oxygen-vacancy approach are then correlated when both of them result in identical

thickness dependence. This result also implies that one of the origins for the enhanced coupling coefficient is the presence of oxygen vacancies concentrated near the electrode/film interface. Secondly, the change of the coupling coefficient along the thickness direction, as induced by oxygen vacancies, is smoothly varying, instead of step-wise. Consequently, the distributed coupling coefficient gives a better fitting of experiment.

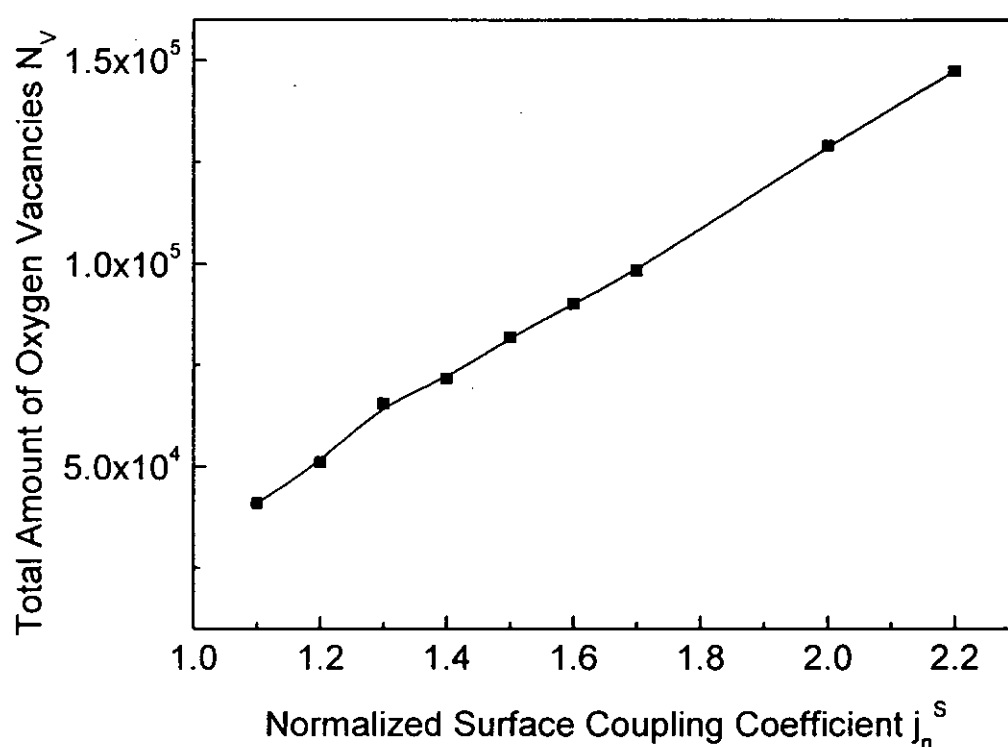


Fig. 5.7 Relation between the number of oxygen vacancies N_v against and the surface coupling coefficient j_n^s .



From our present simulation, the presence of oxygen vacancies results in the decreasing trend of coercive field. On the other hand, in the presence of depolarization effect, the coercive field increases with thickness when the latter is small. These two are competing influences. Experiments from magnetism [15, 16] and ferroelectric PVDF films [14] confirmed the existence of an increasing trend for small thickness. However, such trend has never been reported in PZT and SBT films from experiments. To solve this puzzle, it is desirable to manipulate these influencing factors. The depolarizing effect cannot be eliminated because of the discontinuity in polarization across the electrode/film interface. The remaining one is the control of the quantity of oxygen vacancies. This is of course a matter of growing a quality film. Oxygen vacancies are always present during the formation of electrode. By the suitable selection of electrode material, the influence of oxygen vacancies can be kept to minimal. Under this situation, the increasing trend is expected to appear.

5.6 Simulation Results on Polarization Fatigue and Coercive Field Enhancement

Polarization fatigue is a phenomenon that the switchable polarization is gradually reduced after a number of switching cycles. Moreover, the reduction increases with the number of cycles. Recently, some experiments suggested that the reduction of switchable polarization and enhancement of coercive field occur simultaneously [4, 29]. Most of the investigators have focused on the reduction of polarization, while overlooking both the effect and the origin for the enhancement of coercive field. In fact, oxygen vacancies can



migrate into the film through the electrodes, so that their quantity increases with time. This increase suppresses the remanent polarization on one hand, and enhanced the coercive field on the other. In our present work, we have simulated a set of hysteresis loops with different total number of oxygen vacancies. From these loops, we can determine both the coercive and remanent polarization. After that, we can plot the coercive field e_c and remanent polarization p_r against different total number of oxygen vacancies N_v as shown in Fig. 5.8. It demonstrates that polarization fatigue is associated with the accumulation of oxygen vacancies through the diffusion from electrodes. Similar suggestion has been presented elsewhere in literature [34].

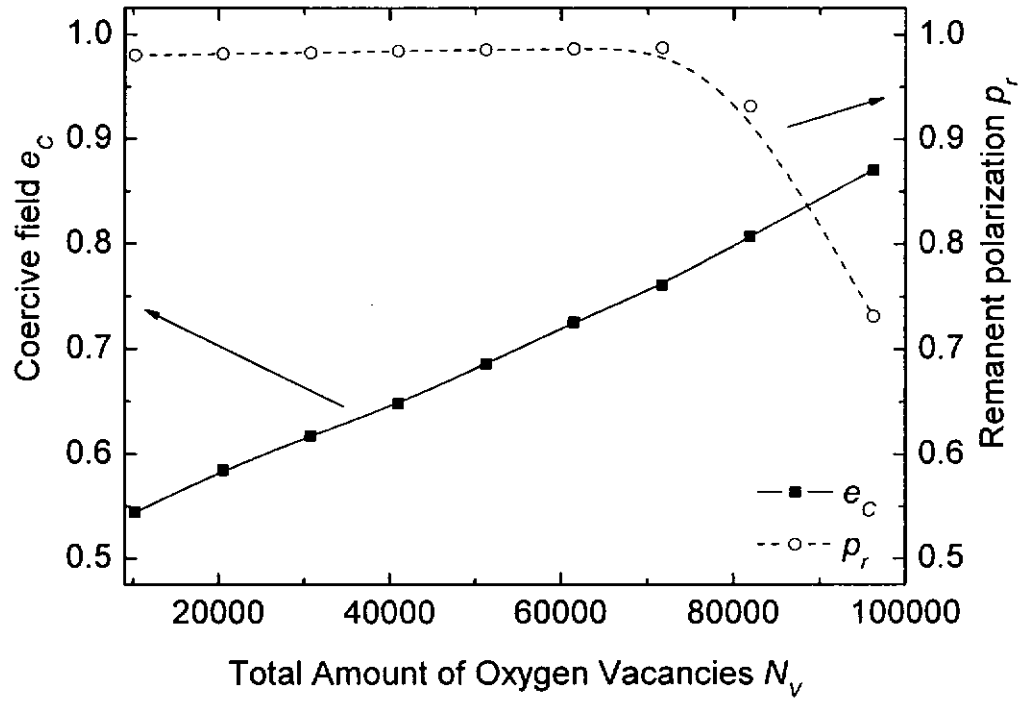


Fig. 5.8 Plot of coercive field e_c and remanent polarization p_r against the total number of oxygen vacancies N_v .

Oxygen vacancy is a hole trapper [35, 60], establishing a trapping level inside the energy band gap. It traps a hole when the position of Fermi level is below the trapping level but it releases a hole again when the positions of these two levels are reversed, as shown in Fig. 5.9. There are two different charge states for oxygen vacancy: the neutral species V^x and the singly-charged one V^+ . The trapping and detrapping of hole by a neutral species can be expressed by the following reaction:



The population of charged oxygen vacancies N_v^+ is related to the total number of oxygen vacancies by Eqn. (5.4) and Eqn. (5.5).

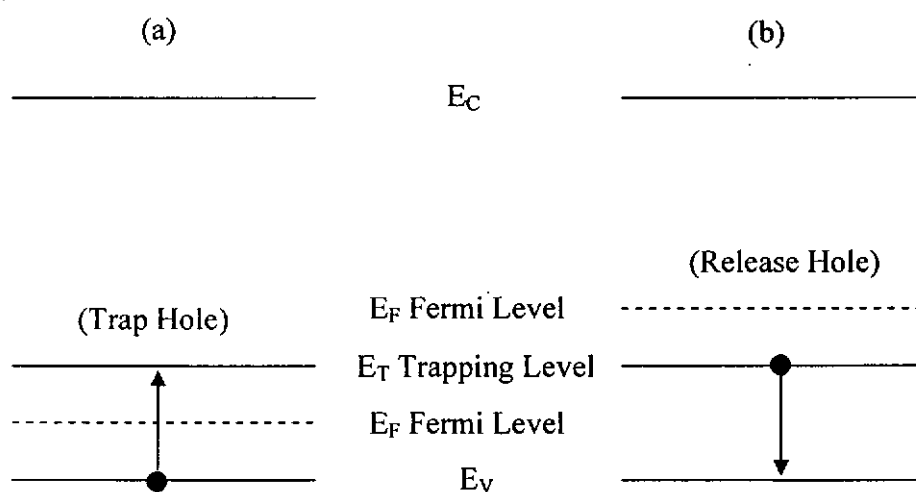


Fig. 5.9 A trapping level is induced by an oxygen vacancy. (a) It traps a hole when the position of Fermi level is below, and (b) releases a hole when the Fermi level is above the trapping level.



Considering an alternating driving voltage in the form of a sequence of square pulses, the period Γ is the reciprocal of the pulse repetition rate (PPR). The pulse width is exactly one-half of the period. Initially, all vacancies are in neutral uncharged state (untrapped), and $N_v^+ = 0$. During the application of the first pulse, hole-trapping takes place. The rate of increase of N_v^+ is governed by the following relation:

$$\frac{dN_v^+}{dt} = \sigma_t(N_v - N_v^+) - e_t N_v^+, \quad (5.15)$$

where σ_t and e_t are, respectively, the capture and emission rates of the holes by the oxygen vacancy. It is a generic one which could also be applicable to many other species. There are experimental evidences that the trapping of charge carriers by oxygen vacancies is responsible for the polarization fatigue. Scott *et al.* [31] revealed the depletion of oxygen composition and hence the accumulation of oxygen vacancies after repeated switching cycles, as compared with the virgin sample. Moreover, Al-Shareef *et al.* [36] have induced the fatigue behavior in Strontium Bismuth Tantalate with metal electrodes (Pt/ SBT/ Pt) and Lead Zirconate Titanate with oxide electrodes (LSCO/ PZT/ LSCO) under UV illumination. These two systems were supposed to be fatigue free under normal switching condition. The fatigue behavior was attributed to the pinning of domain walls by the increased charge trapping rate in the presence of UV illumination. Obviously, the trapping of charge carriers by oxygen vacancies is an essential condition for the occurrence of polarization fatigue.



During the application of filling pulse, the first term dominates, and the second term is ignored for simplicity. At the end of the filling pulse, the gain in charged vacancies becomes

$$N_v^+ = N_v \{1 - \exp(-\sigma_i \Gamma / 2)\} + N_v^+(0) \exp(-\sigma_i \Gamma / 2). \quad (5.16)$$

where $N_v^+(0)$ is the initial number of oxygen vacancies in positively charged state. At the second half of a cycle, part of the holes is released from the traps as described by:

$$\frac{dN_v^+}{dt} = -e_i N_v^+. \quad (5.17)$$

If the trapping rate is larger than the detrapping rate, there must be a gain in charged oxygen vacancies at the end of each cycle. For instance, after the first cycle, the number of charged oxygen vacancies becomes

$$N_v^+(1) = \{N_v [1 - \exp(-\sigma_i \Gamma / 2)] + N_v^+(0) \exp(-\sigma_i \Gamma / 2)\} \exp(-e_i \Gamma / 2) > N_v^+(0). \quad (5.18)$$

Where “(1)” on the left hand side of Eqn. (5.18) denotes the first cycle. After a number of repetitive pulses, the gain in this charged species is denoted by $N_v^+(N)$. The increase in space charge is then related by $\Delta Q = q N_v^+(N)$. The relation between ΔQ and the number of switching cycles is shown in Fig. 5.10. By fitting the asymptotic line of ΔQ against frequency f , ΔQ is inversely proportional to the frequency governed by the following relation $\Delta Q = q c_3 N^{0.25} / f$, where c_3 is a constant, and N the number of switching cycles. From Eqn. (5.6), the local charge density depends on both the number of switching cycles and the frequency through the following relation:

$$\rho_{sc} = \frac{qc_s N^{0.25}}{N_x(\Delta z)f} f(z) = q_r f(z). \quad (5.19)$$

The frequency dependence of polarization fatigue is then indirectly caused by the frequency dependence of space charge.

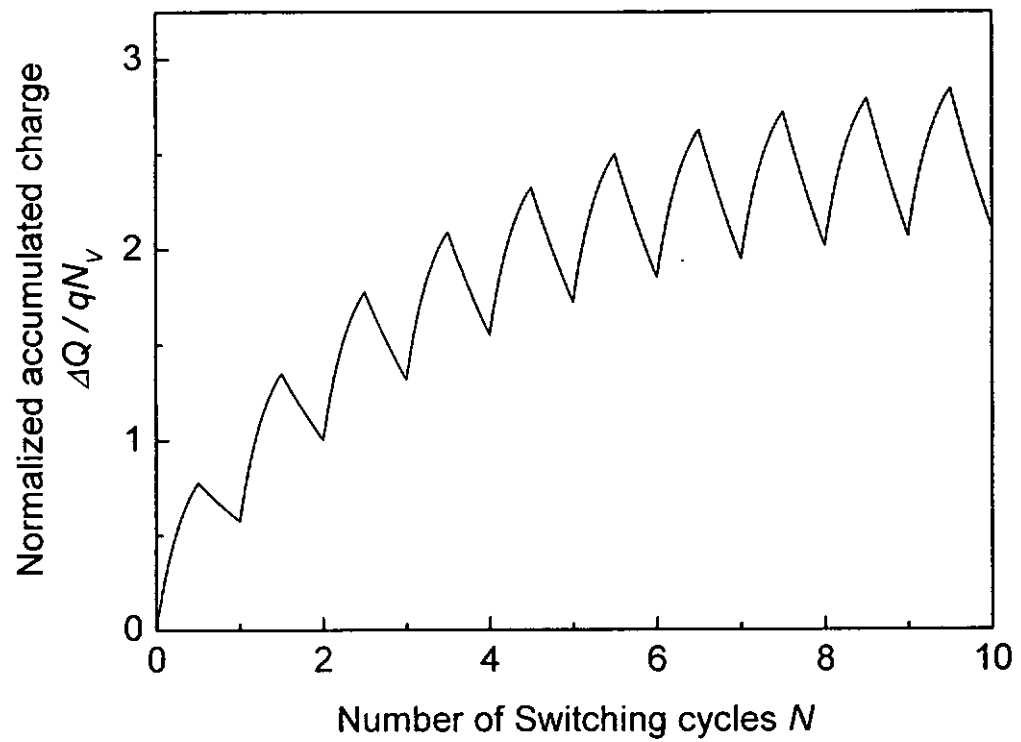


Fig. 5.10 The plot of accumulated charge $\Delta Q / qN_v$ against number of switching cycles N .
 $(\Gamma_{MCS} = 300\text{MCS}, \sigma_r = 0.01\text{MCS}^{-1}, e_r = 0.002\text{MCS}^{-1})$



Based on the switching-cycle and frequency dependent space charge expressed in Eqn. (5.19), we can simulate the temperature, amplitude of the driving voltage and frequency dependences of polarization fatigue. The simulated results are compared with experiments as follows:

The effect of temperature is shown in Fig. 5.11, where our simulation result and the experimental result of Paton *et al.* [61] are represented by curves and symbols, respectively. At the temperature of 200K, the trends from both theory and experiment agree quite well. The deviation becomes large for 300K and 500K. This deviation might be due to the omission of temperature dependence of the population of charged vacancies. Moreover, the trapping and detrapping rate of holes by these vacancies are also temperature dependent, which has been omitted in our present model, for simplicity. Nevertheless, the experimentally observed temperature effect has been qualitatively reproduced, i.e. the larger the ambient temperature, the faster decay of remanent polarization occurs.

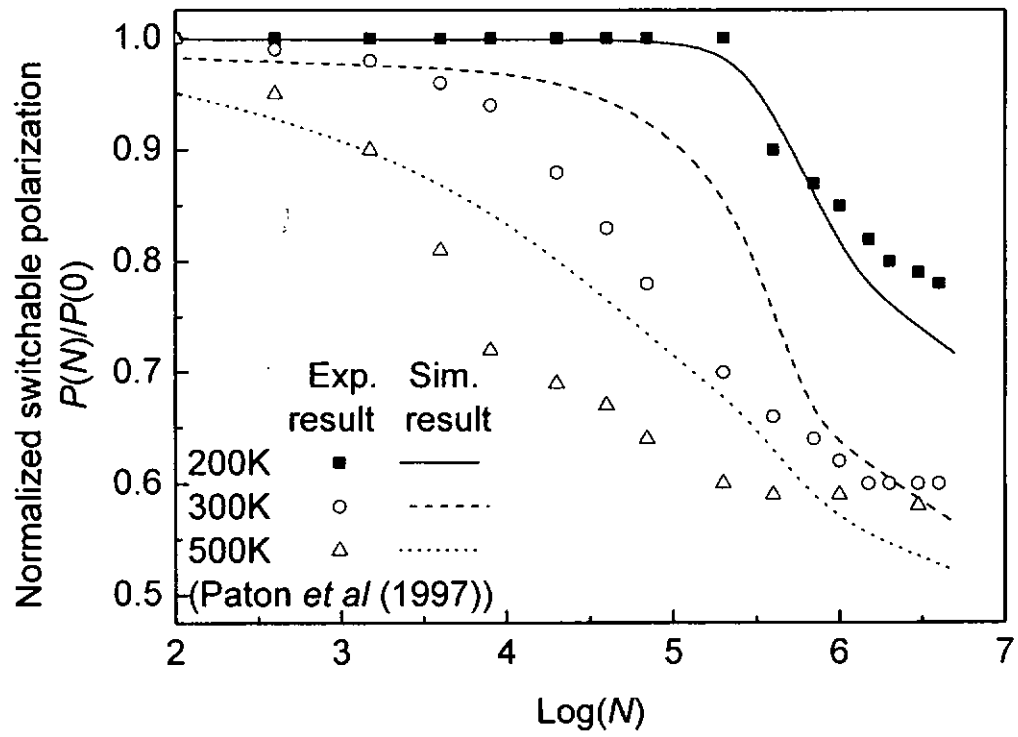


Fig. 5.11 Effect of temperature on polarization fatigue: our simulated results are plotted as curves; experimental results from Pantou *et al.* [61] are shown as symbols.

Fig. 5.12 shows the effect of the amplitude of the driving voltage, where the experimental results of Mihara *et al.* [52] and our simulation result are represented by symbols and curves, respectively. The agreement between both results is quite well. It is envisaged that the polarization decays faster for a smaller amplitude. In the presence of oxygen vacancies, an additional energy is expensed to switch the dipole in favor of the driving voltage. A low driving voltage does not acquire enough energy to switch the dipole and the portion of unswitchable dipoles increases.

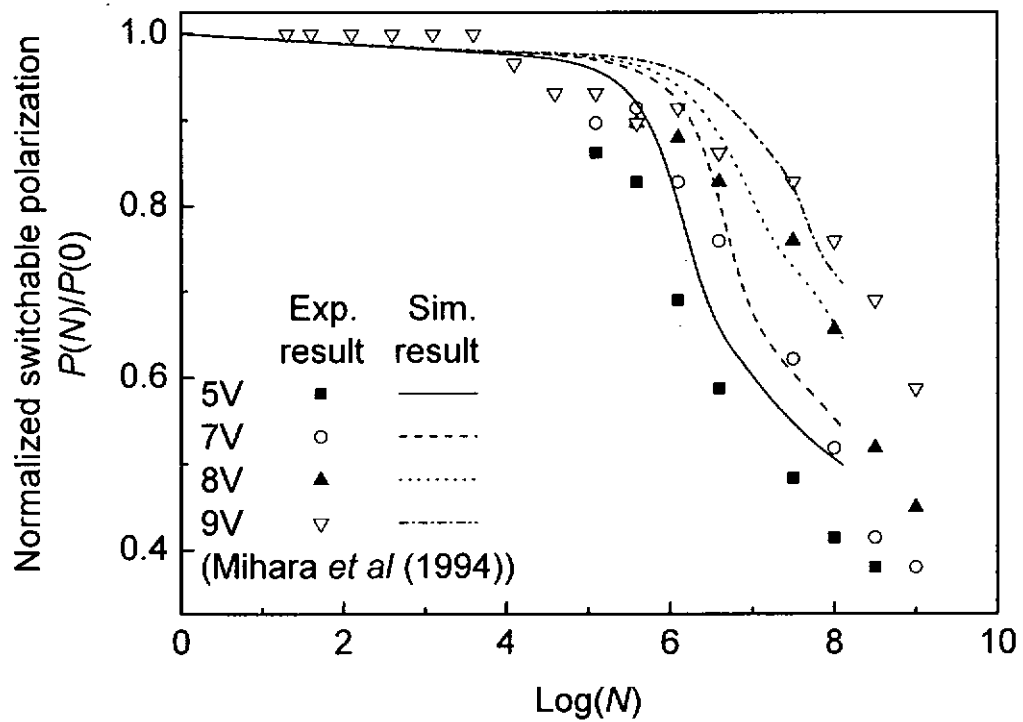


Fig. 5.12 Effect of amplitude of driving voltage on polarization fatigue: our simulated results are plotted as curves; experimental results from Mihara *et al.* [52] are shown as symbols.

Fig. 5.13 shows the effect of the frequency, the simulated result (curves) and experimental result from Majumder *et al.* [29] (symbols). Agreement between theory and experiment is quite good for both 100Hz and 1kHz. There is a discrepancy at 100kHz. The polarization fatigue derived from theory occurs much faster than observed from experiment. One of the possible causes for this discrepancy is that the quantity of oxygen vacancies in our present model is constant, even though the charged species increases with N . If one considers the gradual increase in the quantity of oxygen vacancies due to diffusion, the resultant fatigue rate should be much slower. Despite this discrepancy, the qualitative trend of frequency dependence can be reproduced.

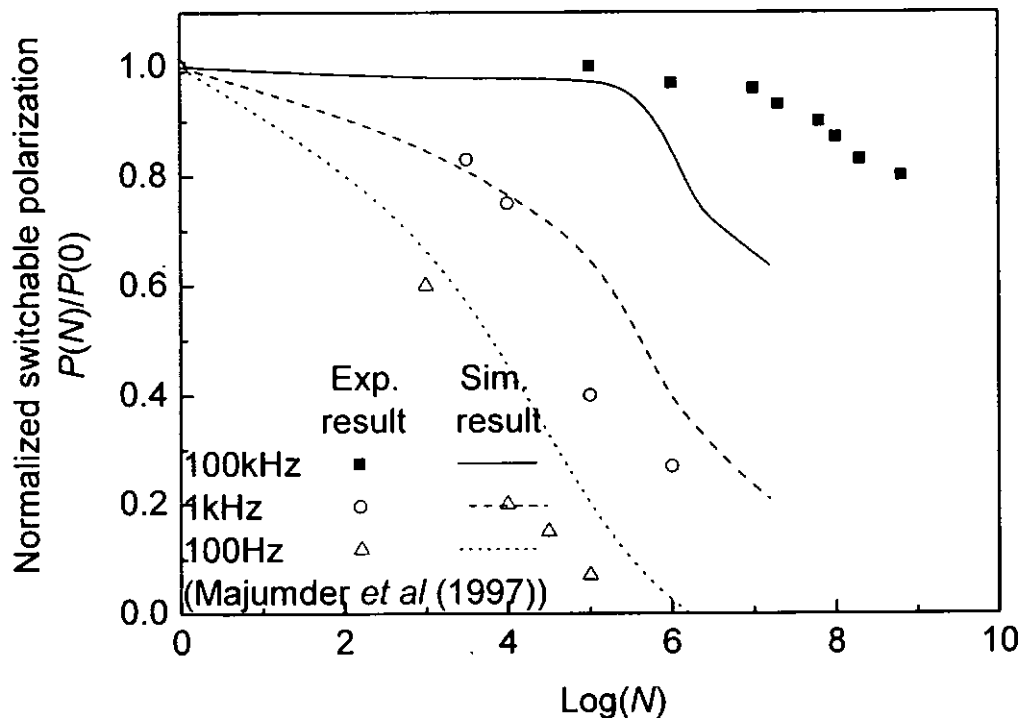


Fig. 5.13 Effect of frequency on polarization fatigue curves: simulated result; symbols: experimental result from Majumder *et al.* [29].



Polarization fatigue as a cause of the trapping of charges by oxygen vacancies has been presented elsewhere [29, 34]. Dawber *et al.* [34] suggested that the switchable polarization $P(N)$ are inversely proportional to the concentration of oxygen vacancies, they did not explain how this relation was derived. On the other hand, Majumder *et al.* [29] have merely provided a fitted relation from experimental result. In our present work, we derived the relation of the charged vacancies with frequency and switching cycles from the imbalance of charge trapping and detrapping from each cycle. These charged vacancies are responsible for the polarization fatigue.

In this chapter, the trapping rate σ_t and the detrapping rate e_t have been kept constant throughout our simulation. In reality, both of them are temperature dependent. Consequently, a better simulation result can be obtained by considering the temperature dependent trapping and detrapping rates.

Oxygen vacancy is quite a mobile species. Thus, the distribution function of oxygen vacancies along the thickness direction can vary with time. However, in our present work, the distribution function $f(z)$ is independent of the switching cycles. A further improvement of our present model is to incorporate a time-dependent distribution function caused by the diffusion of oxygen vacancies.

It can be found in some experiments that enhancement [4, 35] of coercive field occurs during the polarization fatigue while others show opposite result [36, 37]. Our simulation result shows only the enhancement. Obviously, the enhancement of coercive field must be caused by the presence of oxygen vacancies. Alternatively speaking, there might be many species responsible for the polarization fatigue. The enhancement of



coercive field during the polarization fatigue can be regarded as an evidence for the presence of oxygen vacancies. The other origins causing the polarization fatigue, for example, the formation of surface layer with a lower dielectric permittivity [4], depletion of charge carrier [38], or existence of microcracks [39], can only reduce the coercive field.



CHAPTER VI

CONCLUSION

In this project, the thickness dependences of both coercive field and remanent polarization in ferroelectric films have been numerically simulated using four-state Potts model. The major cause for these dependences is attributed to the distributed oxygen vacancies, concentrated near the electrode/film interface. The role of oxygen vacancy has also been discussed. On one hand, in the presence of an oxygen vacancy in a perovskite cell, the displacement of the B-site cation (for example Ti^{4+}) about the centre of the cell becomes asymmetric. An additional energy is required to displace the cation from one meta-stable equilibrium state to the other. On the contrary, the reverse displacement releases the same amount of energy. This picture has been recognized as domain-wall pinning during the polarization switching. This effect can be effectively reflected by adopting larger coupling coefficient between dipoles in the presence of oxygen vacancies. On the other hand, the oxygen vacancy is also a hole trapper, resulting in the gradual increase in space charge as the switching proceeds.

In the presence of the distributed oxygen vacancies in a film, the experimental thickness dependences of coercive field and remanent polarization reported by Fujisawa *et al.* [9] can be reproduced numerically. The origin of polarization fatigue has also been discussed. There are a number of explanations and the presence of oxygen vacancies is only one of them. However, in some experiments, it was found that the enhancement of coercive field is associated with the polarization fatigue. This feature can be successfully



explained by the effect imposed by oxygen vacancies. The experimental results of temperature, amplitude of the switching voltage, and frequency dependences of the polarization fatigue have also been simulated.



REFERENCE

- [1] J. F. Scott, *Ferroelectric Memories*, Springer (2000).
- [2] K. R. Udayakumar, P. J. Schuele, J. Chen, S. B. Krupanidhi, and L. E. Cross, *J. Appl. Phys.*, **77**, 3981 (1995).
- [3] J. Zhu, X. Zhang, Y. Zhu, and S. B. Desu, *J. Appl. Phys.*, **83**, 1610 (1998).
- [4] W. L. Warren, D. Dimos, B. A. Tuttle, G. E. Pike, R. W. Schwartz, P. J. Clews, and D. C. McIntyre, *J. Appl. Phys.*, **77**, 6695 (1995).
- [5] A. Q. Jiang, J. F. Scott, M. Dawber, and C. Wang, *J. Appl. Phys.*, **92**, 6756 (2002).
- [6] H. M. Duiker, P. D. Beale, J. F. Scott, C. A. Pas de Araujo, B. M. Melnick, J. D. Cuchiaro, and L. D. McMillan, *J. Appl. Phys.*, **68**, 5783 (1990).
- [7] C. H. Park and D. J. Chadi, *Phys. Rev. B*, **57**, 13961 (1998).
- [8] V. C. Lo, *J. Appl. Phys.*, **92**, 6778 (2002).
- [9] H. Fujisawa, S. Nakashima, K. Kaibara, M. Shimizu, and H. Niu, *Jpn. J. Appl. Phys.*, **38**, 5392 (1999).
- [10] C. H. Lin, P. A. Friddle, C. H. Ma, A. Daga, and H. Chen, *J. Appl. Phys.*, **90**, 1509 (2001).
- [11] T. K. Kundu and J. Y.-M. Lee, *Jpn. J. Appl. Phys.*, **39**, 3488 (2000).
- [12] G.-F. Huang and S. Berger, *J. Appl. Phys.*, **93**, 2855 (2003).
- [13] J. Zhu, X. Zhang, Y. Zhu, and S. B. Desu, *J. Appl. Phys.*, **83**, 1610 (1998).
- [14] S. Ducharme, V. M. Fridkin, A. V. Bune, S. P. Palto, L. M. Blinov, N. N. Petukhova, and S. G. Yudin, *Phys. Rev. Lett.*, **84**, 175 (2000).



- [15] T. Chang, J.-G. Zhu, and J. H. Judy, *J. Appl. Phys.*, **73**, 6716 (1993).
- [16] M. S. Wei and S. Y. Choi, *J. Appl. Phys.*, **76**, 6679 (1994).
- [17] J. Junquera and P. Ghosez, *Nature*, **422**, 506 (2003).
- [18] H. Kohlstedt, N. A. Pertrev, and R. Waser, *Mat. Res. Soc. Symp. Proc.*, **688**, C.6.5 (2002).
- [19] L. M. Blinov, V. M. Fridkin, S. P. Palto, A. V. Bune, P. A. Downen, and S. Ducharme, *Phys. Usp. Fiz. Nauk.*, **43**, 243 (2000).
- [20] A. K. Taganstev and I. A. Stolichnov, *Appl. Phys. Lett.*, **74**, 1326 (1999).
- [21] P. K. Larsen, G. J. M. Dormans, D. J. Taylor, and P. J. van Veldhoven, *J. Appl. Phys.*, **76**, 2405 (1994).
- [22] L. Baudry and J. Tournier, *J. Appl. Phys.*, **90**, 1442 (2001).
- [23] W. Ma, M. Zhang, L. Sun, Y. Chen, N. Ming, Y. Jin, and Q. Huang, *Ferroelectr. Lett. Sect.*, **23**, 153 (1998).
- [24] A. K. Tagantsev, I. Stolichnov, E. L. Colla, and N. Setter, *J. Appl. Phys.*, **90**, 1387 (2001).
- [25] V. C. Lo, *J. Appl. Phys.*, **94**, 3353 (2003).
- [26] H. L. Richards, M. Kolesik, P. A. Lindgrad, P. A. Rivold, and M. A. Novotny, *Phys. Rev. B*, **55**, 11521, (1997).
- [27] L. Mitoseriu, D. Ricinchi, C. Harbageea, M. Okuyama, T. Tsukamoto, and V. Tura, *Jpn. J. Appl. Phys.*, **35**, 5210 (1996).
- [28] A. V. Bune, V. M. Fridkin, S. Ducharme, L. M. Blinov, S. P. Palto, A. V. Sorokin, S. G. Yudin, and A. Zlatkin, *Nature*, **391**, 874 (1998).



- [29] S. B. Majumder, Y. N. Mohapatra, and D. C. Agrawal, *Appl. Phys. Lett.*, **70**, 138 (1997).
- [30] C. W. Law, K. Y. Tong, J. H. Li, and M. C. Poon, *Thin Solid Films*, **354**, 162 (1999).
- [31] J. F. Scott, C. A. Araujo, B. N. Melnick, L. D. McMillan, and R. Zuleeg, *J. Appl. Phys.*, **70**, 382 (1991).
- [32] L. He and D. Vanderbilt, *Phys. Rev. B*, **68**, 134103 (2003).
- [33] D. Dimos, H. N. Al-Shareef, W. L. Warren, and B. A. Tuttle, *J. Appl. Phys.*, **80**, 1682 (1996).
- [34] M. Dawber and J. F. Scott, *Appl. Phys. Lett.*, **76**, 1060 (2000).
- [35] V. C. Lo, K. H. Wong, and K.S. So, *Thin Solid Films*, **458**, 336 (2003).
- [36] H. N. Al-Shareef, B. A. Tuttle, W. L. Warren, T. J. Headley, D. Dimos, J. A. Voigt, and R. D. Nasby, *J. Appl. Phys.*, **79**, 1013 (1996).
- [37] D. Ricinschi and M. Okuyama, *Integr. Ferro.*, **50**, 149 (2002).
- [38] I-Wei Chen and Y. Wang, *Appl. Phys. Lett.*, **75**, 4186 (1999).
- [39] Q. Y. Jiang, E. C. Subbarao, and L. E. Cross, *J. Appl. Phys.*, **75**, 7433 (1994).
- [40] V. C. Lo and Z. J. Chen, Proceedings of the 2000 12th International Symposium on Applications of Ferroelectrics, 27 July – 2 August, Honolulu, Hawaii, 157 (2000).
- [41] I. Stolichnov, A. Tagantsev, E. Colla, S. Gentil, S. Hiboux, J. Baborowski, P. Muralt, and N. Setter, *J. Appl. Phys.*, **88**, 2154 (2000).
- [42] H. Z. Jin and J. Zhu, *J. Appl. Phys.*, **92**, 4594 (2002).



- [43] V. Nagarajan, I. G. Jenkins, S. P. Alpay, H. Li, S. Aggarwal, L. Salamanca-Riba, A. L. Roytburd, and R. Ramesh, *J. Appl. Phys.*, **86**, 595 (1999).
- [44] J.-M. Liu, C. K. Ong, and L. C. Lim, *Ferroelectrics*, **299**, 77 (1999).
- [45] H. Qian and L. A. Bursill, *Int. J. Mod. Phys. B*, **10**, 2027 (1996).
- [46] J.-M. Liu, H. P. Li, C. K. Ong, and L. C. Lim, *J. Appl. Phys.*, **86**, 5198 (1999).
- [47] F. Y. Wu, *Rev. Mod. Phys.*, **54**, 235 (1982).
- [48] S. Tsunekawa, T. Fukuda, T. Ozaki, Y. Yoneda, T. Okabe, and H. Terauchi, *J. Appl. Phys.* **84**, 999 (1998).
- [49] D.-J. Kim, J.-P. Maria, A. I. Kingon, and S. K. Streiffer, *J. Appl. Phys.*, **93**, 5568 (2003).
- [50] F. Xia, H. Xu, F. Fang, B. Razavi, Z.-Y. Cheng, Y. Lu, B. Xu, and Q. M. Zhang, *Appl. Phys. Lett.*, **78**, 1122 (2001).
- [51] C. L. Wang and S. P. R. Smith, *J. Phys.: Condens. Matter*, **8**, 4813 (1996).
- [52] T. Mihara, H. Watanabe, and C. A. Pas de Araujo, *Jpn. J. Appl. Phys.*, **33**, 5281 (1994).
- [53] S. W. Sides, P. A. Rikvold, and M. A. Novotny, *Phys. Rev. E*, **58**, 2710 (1999).
- [54] C. L. Wang, S. R. P. Smith, and D. R. Tilley, *J. Phys.: Condens. Matter*, **6**, 9633-9646 (1994).
- [55] K. T. Li and V. C. Lo, *Solid State Communications*, **132**, 49 (2004).
- [56] S. Horri, S. Yokoyama, H. Nakajima, and S. Horita, *Jpn. J. Appl. Phys.*, **38**, 5378 (1999).
- [57] W. Y. Shih, W. H. Shih, and I. A. Aksay, *Phys. Rev. B*, Vol. **50**, 15575 (1973).



- [58] V. M. Fridkin, Stephen Ducharme, A. V. Bune, S. P. Palto, S. G. Yudin, and L. M. Blinov, *Ferroelectrics*, **236**, 1 (2000).
- [59] S. M. Sze, *Physics of Semiconductor Devices*, 2nd ed. (Wiley, New York, 1981).
- [60] P. F. Baude, C. Ye, and D. L. Polla, *Appl. Phys. Lett.*, **64**, 2670 (1994).
- [61] E. Paton, M. Brazier, S. Mansour, and A. Bement, *Integr. Ferroelectr.*, **18**, 29 (1997).